A Diagnosis of Oceanic Precipitation in IMERG-GMI

Daniel C. Watters[a,b] , George J. Huffman[c] , Patrick N. Gatlin[d] , Pierre-Emmanuel Kirstetter[b,e,f,g] , David T. Bolvin[c,h] , Robert Joyce[c,h] , Eric J. Nelkin[c,h] , Jackson Tan[c,i] , and David B. Wolff[j]

[a] *NASA Postdoctoral Program, NASA Marshall Space Flight Center, Huntsville, Alabama, USA*

[b] *Advanced Radar Research Center, University of Oklahoma, Norman, Oklahoma, USA*

[c] *NASA Goddard Space Flight Center, Greenbelt, Maryland, USA*

[d] *NASA Marshall Space Flight Center, Huntsville, Alabama, USA*

[e] *School of Civil Engineering and Environmental Sciences, University of Oklahoma, Norman, Oklahoma, USA*

[f] *School of Meteorology, University of Oklahoma, Norman, Oklahoma, USA*

[g] *NOAA/National Severe Storms Laboratory, Norman, Oklahoma, USA*

[h] *Science Systems and Applications, Inc., Lanham, Maryland, USA*

[i] *University of Maryland, Baltimore County, Baltimore, Maryland, USA*

[j] *NASA Wallops Flight Facility, Wallops Island, Virginia, USA*

Corresponding author: Daniel C. Watters, daniel.watters@ou.edu

ABSTRACT: Diagnosing errors in spaceborne oceanic precipitation estimates is difficult due to complicated multi-satellite algorithms and limited surface-based measurements. The Global Precipitation Measurement (GPM) mission helps to alleviate these challenges with NASA's Integrated Multi-satellitE Retrievals for GPM (IMERG) product, which is transparently designed to encourage community validation activities, and the GPM Validation Network, which collects observations across global precipitation regimes from over 100 ground-based weather radars to serve as reference datasets for the GPM precipitation products. This study uses the GPM Validation Network's oceanic precipitation observations from 32 island and coastal radars to diagnose the performance of IMERG V06B & V07B Final Run products during GPM Microwave Imager (GMI) overpasses (i.e., IMERG-GMI) in the period June 2014 – September 2021. Errors are traced from the input Level-2 (satellite footprint) Goddard Profiling Algorithm climate (GPROF-CLIM) GMI product through the successive gridding, calibration and precipitation distribution restoration steps of IMERG's Level-3 (gridded) algorithm. Results highlight that IMERG-GMI V07B outperforms V06B in detecting and quantifying oceanic precipitation, with a significant improvement over high-latitude ocean (V06B: +143%; V07B: +50%). Furthermore, there is a clear oceanic latitudinal trend in the mean relative bias of IMERG-GMI V07B (high-latitude: +50%; mid-latitude: +10%; tropical: −41%), which largely traces back to GPROF-CLIM V07 (high-latitude: +22%; mid-latitude: −8%; tropical: −44%), with bias differences driven by IMERG's passive microwave calibration scheme. This error tracing approach supports future IMERG algorithm developments by disentangling how algorithm steps enhance or mitigate errors.

SIGNIFICANCE STATEMENT: Most precipitation occurs over ocean, yet precipitation products are rarely evaluated there due to a lack of surface-based measurements. This study utilizes the GPM Validation Network's datasets from coastal and island radars to conduct the first oceanic evaluation of the NASA IMERG V07B multi-satellite precipitation product. The performance of IMERG at different successive algorithm steps is assessed to understand which processing steps reduce or increase errors and to support future algorithm improvements. The latest IMERG version provides more accurate and reliable precipitation estimates than the preceding version. However, IMERG-GMI is biased high by +50% and low by −41% over the high-latitude and tropical oceans, respectively.

1. Introduction

Precipitation is the paramount component of the water cycle, delivering ~554,000 km^3 of water in a variety of states to Earth's surface every year (e.g., rain, snow, hail, graupel, etc.; Allan et al. 2020; Tapiador et al. 2017). This critical source of freshwater supports life on Earth, yet society can also be victim to the destructive nature of precipitation extremes, such as droughts, tropical cyclones and floods. Consequently, scientists strive to improve the accuracy of global precipitation estimates from satellite constellation observations (Levizzani et al. 2020a,b). However, the current uncertainty in global precipitation observations, and the equivalent latent heat flux which precipitation observations help to constrain within Earth's energy budget (Stephens et al. 2012; Wild et al. 2015; L'Ecuyer et al. 2015; Adler et al. 2020), hampers our full understanding of climate responses to global warming.

The bias in oceanic precipitation estimates is a key limitation of present global precipitation estimates. Stephens et al. (2012) approximated the uncertainty in annual mean oceanic precipitation to be between ±10% and ±20% from a variety of studies (Petty 1997; Dai et al. 2007; Haynes et al. 2009; Ellis et al. 2009; Berg et al. 2010). Subsequently, to achieve balance in their approximation of the global energy budget, Stephens et al. (2012) increased global precipitation (and latent heat flux) from the Global Precipitation Climatology Project (GPCP; Adler et al. 2003) Version-2 (V2) multi-satellite product by >10% to account for oceanic and snowfall deficiencies. Furthermore, studies by Behrangi et al. (2014, 2024) and Behrangi and Song (2020) have consistently found that GPCP underestimates global mean oceanic precipitation (V2.2: −4%; V2.3: −9%; V3.2:

−6.5%). However, spaceborne underestimation of oceanic precipitation is not limited to GPCP alone, and uncertainty in oceanic precipitation amongst global precipitation products is particularly problematic in the mid- and high-latitudes (Behrangi et al. 2024; Behrangi and Song 2020). With ∼78% of global precipitation falling over the oceans (Trenberth et al. 2007; Allan et al. 2020), increasing the accuracy and precision of satellite-based oceanic precipitation observations is a critical step toward constraining global precipitation.

Evaluating errors in oceanic precipitation retrieved from instantaneous satellite observations requires two challenges to be addressed. The first challenge is identifying surface-based observations of oceanic precipitation at fine spatiotemporal resolutions with extensive spatiotemporal coverage; this is a notorious problem, as such precipitation measurements are difficult to obtain. Previous studies have assessed spaceborne oceanic precipitation estimates by utilizing reference sensors such as passive aquatic listeners (Bytheway et al. 2023; Li et al. 2023), buoys (Prakash et al. 2018; Khan and Maggioni 2019; Bolvin et al. 2021; Pradhan and Markonis 2023), shipborne sensors including radar and disdrometer (Kucera and Klepp 2022; Montoya Duque et al. 2023), and coastal and island-based radars (Derin et al. 2021, 2022; Wang et al. 2022), though without an ideal combination of volumetric (non-point) observations at a wide range of consistent locations across multiple oceans spanning multiple years. The second challenge in evaluating spaceborne oceanic precipitation estimates is diagnosing errors within the complicated multi-satellite algorithms used to produce them. Multi-satellite algorithms typically include a range of merging, interpolation, intercalibration and/or bias adjustment schemes (Adler et al. 2003; Huffman et al. 2020b, 2023a,c; Kubota et al. 2020; Joyce et al. 2004; Xie et al. 2017), and fully disentangling the effects of these schemes is not always possible.

The NASA-JAXA Global Precipitation Measurement mission (GPM; Hou et al. 2014; Skofronick-Jackson et al. 2017; Kidd et al. 2020; Watters and Battaglia 2021a,b) has the potential to improve our quantification of global oceanic precipitation by alleviating the aforementioned challenges. GPM has provided global observations of rain and snow from space since February 2014 via an international satellite constellation, which is calibrated by the GPM Core Observatory's (CO) Dual-Frequency Precipitation Radar (DPR) and GPM Microwave Imager (GMI) instruments (Iguchi et al. 2018; Battaglia et al. 2020; Berg et al. 2016; Wentz and Draper 2016; Skofronick-Jackson et al. 2018). NASA's most-popular GPM product, Integrated Multi-satellitE

Retrievals for GPM (IMERG; Huffman et al. 2023c, 2020b), provides a global-gridded precipitation record spanning more than 24 years which informs many downstream applications including hurricane analyses (Watters and Battaglia 2021b; Petersen et al. 2020), diurnal cycle research (O and Kirstetter 2018; Watters and Battaglia 2019; Battaglia et al. 2019; Tan et al. 2019; Hayden and Liu 2021; Hayden et al. 2023; Ramadhan et al. 2024; Dai 2024), hydrological modeling (Woods et al. 2023a,b, 2024), climate model evaluation (Watters et al. 2021), insurance modeling, disease exposure forecasts, disaster response and recovery, amongst many others (Portier et al. 2023; Kirschbaum et al. 2017; Skofronick-Jackson et al. 2017, 2018). The U.S. GPM Science Team produces IMERG by intercalibrating, merging and interpolating all GPM constellation microwave (MW) precipitation estimates, with spaceborne infrared (IR) precipitation estimates helping to fill MW-sparse regions and precipitation gauge analyses constraining spaceborne precipitation estimates over land, respectively. IMERG outputs global precipitation fields from successive algorithm operations in a transparent design to enable community ground validation activities and support algorithm developments.

NASA also provides surface-based oceanic precipitation observations from the GPM Validation Network (VN; Schwaller and Morris 2011; Gatlin et al. 2020) which, together with the diagnosable IMERG multi-satellite product, support a thorough investigation of oceanic precipitation. NASA's GPM VN software system performs three-dimensional collocated matchups between the GPM-CO sensors and surface-based radar observations, obtained from over 100 operational and research radars situated across the contiguous U.S. (CONUS), Alaska, Brazil, Australia and tropical islands (NASA 2015). The GPM VN's surface-based radar datasets cover a wide range of latitudes and precipitation climatologies and are subject to consistent precipitation retrievals and quality control procedures; hence, the GPM VN constitutes the most climatologically-diverse network of surface-based radars for satellite precipitation enhancement. Consequently, the VN provides an ideal oceanic validation testbed for evaluating IMERG when GMI overpasses occur (i.e., IMERG-GMI).

In this study, we conduct an error tracing diagnosis of IMERG-GMI Final Run's oceanic precipitation by utilizing the GPM VN across 7+ years of the GPM era (June 2014 – September 2021). Error tracing through multi-satellite algorithms is critical to their advancement, enabling a full diagnosis of what algorithm steps enhance and/or mitigate errors within the Level-3 (gridded) algorithm (i.e., IMERG) as well as the impact of the source Level-2 (satellite footprint) data (i.e., the

Goddard Profiling Algorithm climate / GPROF-CLIM precipitation estimates; Kummerow et al. 2015). Furthermore, error tracing between the preceding and current versions of IMERG-GMI Final Run (V06B and V07B, respectively) is conducted due to a range of significant upgrades including correction of IMERG's 0.1° eastward geolocation gridding offset prior to V07 (Watters et al. 2024), and the introduction of a scheme to mitigate the distortion in the distribution of precipitation fields due to averaging (SHARPEN; Tan et al. 2021) amongst many other updates (Huffman et al. 2024). This analysis considers IMERG performance at GMI overpasses, but not the other GPM passive MW (PMW) constellation and IR sources, because: 1) IMERG performance should be best in these instances as the GMI is the calibration standard of the GPM constellation (Berg et al. 2016; Wentz and Draper 2016; Skofronick-Jackson et al. 2018); and 2) the GPM VN only provides ground radar (GR) matchups with the GPM-CO sensors, and so extending the analysis to other constellation sensors would require efforts well beyond the scope of this study.

This study includes a multitude of advances upon our previous error tracing of IMERG-GMI V06B Final Run's oceanic precipitation estimates using GPM VN V2.3 (Watters et al. 2024). We now evaluate the latest IMERG-GMI V07B estimates using new GPM VN V2.4 data, which provide more accurate GR precipitation rates by including instances of no-rain into the GPM-GR matchups and enable the novel determination of oceanic precipitation detection capabilities by GPROF-CLIM GMI and IMERG-GMI. Another major advancement of this study is the inclusion of more VN GRs; Watters et al. (2024) assessed IMERG against only 6 island GRs located across the Alaskan and tropical oceans, whilst this study utilizes 32 coastal and island GRs including new locations along the CONUS, Alaskan and Brazilian coastlines to conduct the most representative IMERG oceanic precipitation analysis to date. This study is the first oceanic error tracing assessment of IMERG V07 over such a wide range of precipitation climatologies and latitudes.

2. Data

For this IMERG oceanic precipitation error tracing study, five GPM products are required: the IMERG Final Run product (V07B & V06B), the GPROF climate GMI product (V07 & V05), and the GPM VN's GRtoGPROF GMI V2.4 product. Note that there was no GPROF V06 product, as the algorithm directly upgraded from V05 to V07; consequently, IMERG V06B used GPROF V05.

a. IMERG Final Run

IMERG is a Level-3 multi-satellite precipitation product which provides precipitation estimates across the Earth (90°N–S) at high spatial ($0.1° \times 0.1°$) and temporal (30-minute) resolution (Huffman et al. 2023c, 2019b). NASA's IMERG product is available in "Runs" at three different latencies, each successively with more satellite contributions and additional algorithm techniques. The IMERG Runs are designed to support disaster response and weather forecasting (Early Run, latency: $\sim$ 4 hours), public health and insurance applications (Late Run, latency: $\sim$ 14 hours), and research investigations (Final Run, latency: $\sim$ 4.5 months; Kirschbaum et al. 2017; Portier et al. 2023). The Final Run is evaluated in this analysis as it is the most complete algorithm run and hence tends to outperform the lower-latency IMERG Runs (Wang et al. 2020; Mahmoud et al. 2021; Pradhan and Markonis 2023). IMERG Final Run data are available from June 2000 to near-present for V07B, and to September 2021 for the preceding V06B (Huffman et al. 2023b, 2019a).

The IMERG algorithm is underpinned by the GPM satellite constellation, a network of approximately 11 PMW radiometers (at any given time) each traversing around the Earth in various unique polar low-Earth orbits (LEO), that provides quasi-global precipitation coverage on sub-daily timescales (Hou et al. 2014). The underpinning satellite constellation is calibrated by radar and PMW sensors onboard the Tropical Rainfall Measuring Mission satellite (TRMM; Simpson et al. 1996; Kummerow et al. 1998) or the GPM-CO, dependent on the era (TRMM: June 2000 – May 2014; GPM: June 2014 – present; Huffman et al. 2023c). Data from the GPM-CO / TRMM satellite is used to calibrate all other constellation PMW radiometers due to: its inclined, precessing orbit, which enables matchups with all other LEO-PMW sensors; the GMI / TRMM Microwave Imager (TMI), which is superior in accuracy to all other spaceborne PMW radiometers (Berg et al. 2016; Wentz and Draper 2016; Skofronick-Jackson et al. 2018); and the DPR / TRMM Precipitation Radar, which can directly sense precipitation in three dimensions unlike PMW radiometers (Iguchi et al. 2018; Battaglia et al. 2020). Principally, the IMERG Final Run algorithm intercalibrates, merges and interpolates precipitation retrievals from the LEO-PMW radiometer constellation due to the sensitivity of PMW frequency channels to precipitating hydrometeors both within and below the clouds. However, IMERG integrates PMW-calibrated geostationary IR sensor retrievals at times and places when the PMW data are sparse; note that spaceborne IR radiances are representative of cloud tops rather than surface precipitation, and so provide more indirect information

to estimate surface precipitation unlike PMW sensors (Kirstetter et al. 2018, 2020; Petersen et al. 2020). Land-based precipitation gauges are also utilized to make monthly adjustments to the multi-satellite estimates over land.

The key steps in the IMERG V07 Final Run algorithm are outlined below, with an analogous V06 outline provided in Watters et al. (2024). Figure 1 highlights the main changes in IMERG Final Run from V06 to V07 (see Huffman et al. 2024 for an extensive list of V07 updates), and depicts how the precipitation variables associated with these IMERG algorithm steps enable the subsequent error tracing diagnosis.

1. PMW gridding: The PMW constellation footprint precipitation estimates from GPROF-CLIM V07 (Kummerow et al. 2015; NASA 2022) are gridded and combined for each half-hour. IMERG provides no precipitation field output at this algorithm step, but this is recreated in our methodology (Section 3a) and we evaluate this field as variable 'GPROF-CLIM' in the analysis (Section 4).

2. PMW calibration: The gridded PMW precipitation estimates are inter-calibrated to the GPM/TRMM Combined Radar-Radiometer V07 product (CORRA; Olson 2022) in a two-step process. First, the PMW constellation members are climatologically calibrated to the GMI/TMI via a quantile-quantile fit. Second, the GMI/TMI is intercalibrated to CORRA on a dynamic rolling 45-day basis, and then calibration factors are also applied to the PMW constellation members. Prior to PMW calibration, the IMERG algorithm first climatologically adjusts the CORRA V07 estimates to the GPCP V3.2 satellite-gauge product (Huffman et al. 2023a) over high-latitude ocean where CORRA V07 underestimates precipitation (Huffman et al. 2024, 2020a). IMERG provides a precipitation field output at this algorithm step which we evaluate as variable 'IMERG [MW]' in the analysis (Section 4).

3. PMW propagation: The calibrated, gridded PMW estimates are propagated both forward and backward in time to extend the spatial coverage of the LEO-PMW sampling. PMW precipitation features are propagated along motion vectors deduced from reanalysis/model simulations of precipitation, total precipitable liquid water, and total precipitable water vapor (in this hierarchical order; Huffman et al. 2024). Subsequently, the propagated PMW estimates

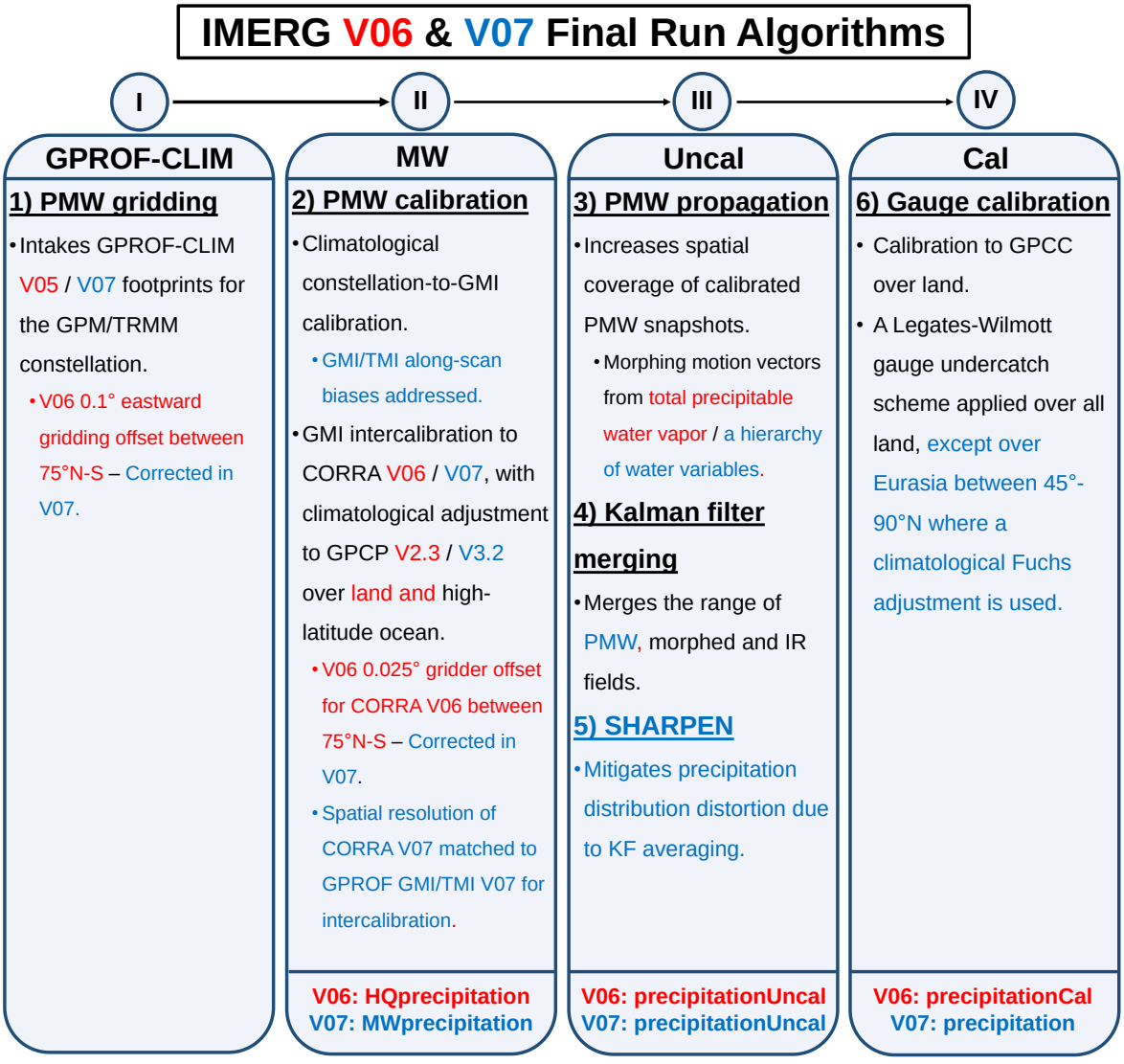

FIG. 1. The workflow for the IMERG V06 and V07 Final Run algorithms. Red and blue font corresponds to steps specific to V06 and V07 only, respectively. Variable 1 (GPROF-CLIM) represents the GPROF-CLIM product subject to the IMERG gridding process, whilst variables 2–4 (MW, Uncal, and Cal, respectively) represent the successive outputs from the IMERG data product. Note that the variable names used within the IMERG data files are located at the bottom of each box, whilst those used for this analysis (Section 4) to ensure consistency in nomenclature between V06 and V07 are listed at the top of each box.

are subject to morphing (a.k.a., quasi-Lagrangian temporal linear interpolation). IMERG provides no precipitation field output at this algorithm step.

4. Kalman filter (KF) merging: The KF merges precipitation estimates from four separate sources at each $0.1^\circ \times 0.1^\circ$ grid box: 1) the CORRA-calibrated PMW estimates from constellation sensors (including the GMI/TMI); 2) the forward-propagated PMW estimates; 3) the backward-propagated PMW estimates; and 4) the PMW-calibrated IR precipitation estimates from geostationary satellites retrieved using the Precipitation Estimation from Remotely Sensed Information using Artificial Neural Networks (PERSIANN) Dynamic Infrared-Rain Rate algorithm (PDIR-Now; Nguyen et al. 2020). IMERG V07 provides no precipitation field output at this algorithm step, but IMERG V06 does which we evaluate as variable 'IMERG [Uncal]' in the analysis (Section 4).

5. SHARPEN: The Scheme to Restore the Distribution of Averaged Precipitation Fields (SHARPEN; Tan et al. 2021) mitigates the distortion of the precipitation rate distribution caused by the KF due to its averaging of precipitation rates from different sources. This procedure adjusts the local KF precipitation rate distribution to one resembling the aggregate of the propagated PMW and IR sources, weighted by their KF contributions. IMERG V07 provides a precipitation field output at this algorithm step which we evaluate as 'IMERG [Uncal]' in the analysis (Section 4), though IMERG V06 does not due to the absence of SHARPEN in this preceding algorithm version.

6. Gauge calibration: Finally, the merged PMW-IR half-hour gridded estimates are calibrated to the gauge-based, undercatch-adjusted Global Precipitation Climatology Centre (GPCC; Schneider et al. 2014) Full/Monitoring product at the monthly scale over land. IMERG provides a precipitation field output at this algorithm step, which we label as 'IMERG [Cal]' though do not evaluate in this analysis (Section 4) due to the lack of gauge calibration over ocean (i.e., IMERG [Cal] equates to IMERG [Uncal] over ocean).

Note that IMERG V07 Final Run underwent a second retrospective reprocessing from V07A to V07B to remove occasional orbits from various constellation PMW sensors that exhibited bad GPROF retrieval values; GMI exhibited no bad orbits, meaning the V05 GPROF-GMI data are all clean as well.

b. GPROF Climate

GPROF-CLIM is a Level-2 precipitation product which provides precipitation estimates for instantaneous snapshots from each PMW radiometer within the GPM constellation, with a spatial resolution of 10.9 km $\times$ 18.1 km for the GMI (the field of view of the 18.7 GHz channel; NASA 2022; Kummerow et al. 2015; Randel et al. 2020; Pfreundschuh et al. 2024). GPROF-CLIM GMI data are available from March 2014 to near-present for V07, and to January 2022 for the preceding V05 (Kummerow 2022, 2017). This parametric Bayesian retrieval algorithm estimates surface precipitation from PMW radiometer measurements of brightness temperature at various frequencies by utilizing an a-priori database of observed precipitation profiles across different surface and environmental conditions. The GPROF V07 a-priori database is principally constructed from CORRA V07 (Olson 2022) over ocean and most land areas, the Ground Validation Multi-Radar Multi-Sensor product (GV-MRMS; Kirstetter et al. 2012, 2014) over snow-covered land, and the ECMWF fifth-generation reanalysis (ERA5; Hersbach et al. 2020) over sea ice. The climate version of GPROF, which underpins the IMERG Final Run algorithm, is produced with a 3-month latency to accommodate the use of a reanalysis (ERA5 in V07; ERA-Interim in V05) for constraining the retrieval.

The GPROF V07 algorithm has undergone several advancements since the preceding V05 algorithm (NASA 2022; Pfreundschuh et al. 2024). Whilst GPROF V05 formed the a-priori database from CORRA V04 and DPR-Ku V04 retrievals over ocean and land/coast, respectively, GPROF V07 upgraded the a-priori source to CORRA V07 over most land and ocean regions (with other sources in snow/ice-surface regions). GPROF V07 has also addressed the lack of orographically-enhanced precipitation in V05 by introducing two new mountain classes in the retrieval scheme whereby the CORRA a-priori precipitation is increased to match ERA5. Spurious coastal precipitation in the previous version of GPROF has been improved by splitting the V05 coast surface class into three new V07 coastal classes.

GPROF-CLIM's *surfacePrecipitation* variable provides the instantaneous surface precipitation rate, and the *precipitationYesNoFlag* variable defines whether there is surface precipitation within the footprint. The *surfaceTypeIndex* variable details the type of surface within the radiometer footprint.

c. GRtoGPROF

The Ground Radar to GPROF (GRtoGPROF) V2.4 Level-2 precipitation product produced by the GPM VN (Schwaller and Morris 2011; Gatlin et al. 2020) provides temporally-coincident GR and GPROF-GMI data spatially matched to the GPROF-GMI footprint resolution (NASA 2015). The GR data are spatially matched to the GPROF-GMI data both along the GMI's line-of-sight slant path and the path perpendicular to the surface for each GR elevation scan (see figures 5.4–1 & 5.4–2 of NASA 2015, respectively), providing three-dimensional GR profiles that statistically summarize (i.e., mean, standard deviation, maximum) the GR variables and retrievals, including radar reflectivity factor, precipitation rate, and hydrometeor classification, within the intersecting field of view (Gatlin et al. 2020). Note that GPROF's precipitation rate estimates are limited to the surface. GR precipitation rates at the GMI footprint scale are constrained to $0.01 \leq R \leq 300\ \mathrm{mm\ h^{-1}}$, with no-precipitation estimates ($R = 0$) retained if the GR measurements are below the precipitation threshold and not contaminated by beam blockage. In the V2.4 matchup process, native-scale GR precipitation rates outside of the $0.01 \leq R \leq 300$ mm $\mathrm{h^{-1}}$ range are no longer excluded from averaging, but instead subject to a statistical method to estimate out-of-range precipitation rates which then are included in the averaging (Helsel and Cohn 1988). Temporal coincidence is ensured by selecting the suite of GR scans for which the start time of the lowest-elevation GR scan falls within ±5 minutes of the GPM-CO's closest approach to the GR.

GRtoGPROF matchups are only produced when precipitation covers ≥1% of the GR vicinity at the time of a GPM-CO overpass, i.e., if the GPM-CO DPR observes precipitation in at least twenty 4-km × 4-km pixels within 100-km range of the GR. Each GRtoGPROF data file provides collocated GR and GPROF data within 125-km range of a select GR site. High-quality polarimetric GR data are ensured by calibration and quality control procedures (Pippitt et al. 2015); in fact, the aggregated suite of GRs have a bias of -0.40 dB (-1.2%) and mean absolute error of 2.28 dB (10.7%) when their radar reflectivity factors are compared to those from the GPM-CO DPR above the freezing level (results not shown; see Warren et al. 2018 and Watters et al. 2018 for details on using the spaceborne DPR to check the calibration of GRs).

At present, the GRtoGPROF V2.4 matchup files are produced for GRs principally located across CONUS, Brazil, Alaska, Australia, Hawaii and other tropical islands, in the period March 2014 – November 2023 (NASA 2024). The 32 VN GRs which provide oceanic measurements and

are used in this analysis are depicted in Figure 2 with further details provided in Table 1. We categorize the oceanic VN GRs into three latitudinal domains (high-latitude, mid-latitude and tropical) based on the Köppen-Geiger climate zones (Beck et al. 2023); note that the southern Floridian GRs (KBYX and KAMX) are categorized as 'tropical' whilst the northern Floridian GRs (KEVX, KTLH, KJAX, KTBW and KMLB) are categorized as 'mid-latitude' due to the transition in Floridian climate zones from tropical (south) to subtropical (north). All oceanic VN GRs are polarimetric and operate at S-band frequency, excluding the C-band polarimetric GR in Darwin, Australia.

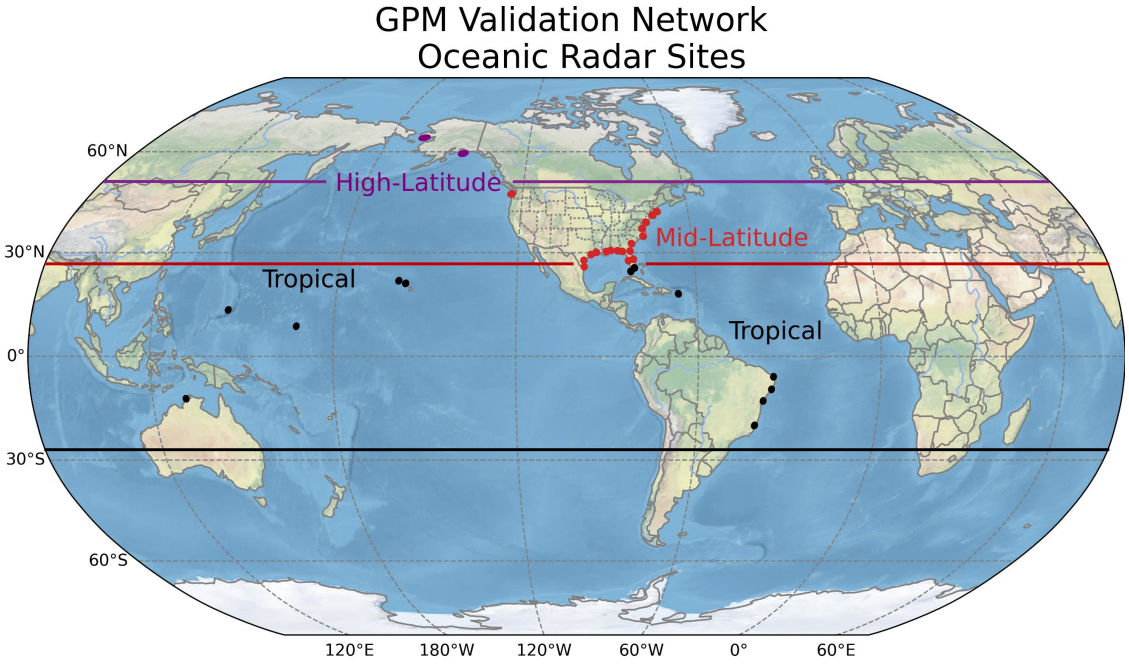

FIG. 2. The GPM Validation Network oceanic radar sites selected for this analysis. The 32 radars are assigned to tropical (12 radars), mid-latitude (18 radars) and high-latitude (2 radars) oceanic domains, informed by the Köppen-Geiger climate zones (Beck et al. 2023). Each circle represents the GR's 125-km radial coverage centered on the GR's location. Further details on the individual GRs can be found in Table 1.

The GPM VN retrieves precipitation rate estimates from the GR measurements using two different algorithms. The Colorado State University Hydrometeor Identification Rainfall Optimization algorithm (CSU-HIDRO; Cifelli et al. 2011) is a dual-polarization radar algorithm which uses the polarimetric measurements and the hydrometeor identification (HID) of the precipitation field to

TABLE 1. A list of the GPM Validation Network's oceanic radar sites selected for this analysis (Figure 2). The number of GPM-CO overpasses when precipitation occurs is limited to the analysis period, June 2014 – September 2021.

Oceanic Domain	Name	Latitude	Longitude	Location	No. of GPM-CO Overpasses
High-Latitude	PAEC	64.5114°N	165.2950°W	Nome, Alaska	924
	PAIH	59.4614°N	146.3030°W	Middleton Island, Alaska	1211
Mid-Latitude	KLGX	47.1158°N	124.1070°W	Langley Hill, Washington	418
	KBOX	41.9558°N	71.1369°W	Taunton, Massachusetts	272
	KOKX	40.8656°N	72.8639°W	Upton, New York	281
	KDOX	38.8256°N	75.4397°W	Dover, Delaware	257
	KAKQ	36.9839°N	77.0072°W	Wakefield, Virginia	10
	KMHX	34.7761°N	76.8761°W	Newport, North Carolina	334
	KCLX	32.6556°N	81.0422°W	Grays, South Carolina	244
	KMOB	30.6794°N	88.2397°W	Mobile, Alabama	303
	KEVX	30.5644°N	85.9214°W	Eglin AFB, Florida	253
	KJAX	30.4847°N	81.7019°W	Jacksonville, Florida	280
	KTLH	30.3975°N	84.3289°W	Tallahassee, Florida	268
	KLIX	30.3367°N	89.8256°W	Slidell, Louisiana	129
	KLCH	30.1253°N	93.2158°W	Lake Charles, Louisiana	265
	KHGX	29.4719°N	95.0792°W	Dickinson, Texas	281
	KMLB	28.1133°N	80.6542°W	Melbourne, Florida	331
	KCRP	27.7842°N	97.5111°W	Corpus Christi, Texas	187
	KTBW	27.7056°N	82.4017°W	Ruskin, Florida	288
	KBRO	25.9161°N	97.4189°W	Brownsville, Texas	197
Tropical	KAMX	25.6111°N	80.4128°W	Miami, Florida	383
	KBYX	24.5975°N	81.7031°W	Boca Chica Key, Florida	389
	PHKI	21.8942°N	159.5520°W	Kauai, Hawaii	302
	PHMO	21.1328°N	157.1800°W	Molokai, Hawaii	257
	TJUA	18.1156°N	66.0781°W	San Juan, Puerto Rico	383
	PGUA	13.4544°N	144.8080°E	Guam	308
	DARW	12.2522°S	131.0430°E	Darwin, Australia	39
	KWAJ	8.7180°N	167.7330°E	Kwajalein, Marshall Islands	474
	NT1	5.9044°S	35.2540°W	Natal, Brazil	147
	MC1	9.5514°S	35.7708°W	Maceio, Brazil	232
	SV1	12.9025°S	38.3267°W	Salvador, Brazil	231
	ST1	19.9888°S	40.5794°W	Santa Teresa, Brazil	56

guide the choice of polarimetric rainfall retrieval. For light precipitation, when the polarimetric measurements can be too noisy, a reflectivity-rain rate (Z–R) relation is often used. The CSU-HIDRO uses a static Z–R relation in these instances. However, the Z–R relation can exhibit much

variability as the overlying microphysical regime changes (Ulbrich and Atlas 1998; Kirstetter et al. 2015). To address this concern, a polarimetrically-tuned Z–R algorithm (Bringi et al. 2004) is also employed which estimates precipitation across the intensity spectrum using $Z = aR^{1.5}$, where a is tuned by polarimetric measurements informing on the drop size distribution. In this analysis, CSU-HIDRO precipitation estimates (VN variable: *GR_RC_rainrate_slantPath*) are selected as the ground reference over tropical and mid-latitude oceans to utilize the most appropriate polarimetric rainfall estimator for moderate and heavy precipitation in these domains. We select the polarimetrically-tuned Z–R precipitation estimates (VN variable: *GR_RP_rainrate_slantPath*) over high-latitude oceans because this algorithm utilizes a varying Z–R relation, which should better depict the prevalent light precipitation intensities there than the constant Z–R CSU-HIDRO relation. Note that precipitation rate estimates are not produced for ice-phase precipitation by either algorithm, and hence ice-phase precipitation is not evaluated in this study. The VN retrieves HID following the Dolan et al. (2013) algorithm, for which freezing level information is imported from the Rapid Update Cycle model over CONUS and the NOAA Global Forecast System elsewhere.

3. Methodology

Gridded precipitation rates from IMERG-GMI Final Run V06B & V07B and GPROF-CLIM V05 & V07 are evaluated against the reference VN GRs over high-latitude, mid-latitude and tropical oceanic regions (Figure 2). This suite of GPM products is analyzed for all GMI precipitating overpass events. The analysis period, June 2014 – September 2021, is chosen for consistency when evaluating IMERG-GMI across multiple versions, as V06B is not available beyond this period. The case study in Figure 3 showcases the gridding process (panels a & b) and error tracing from GPROF-CLIM to IMERG-GMI across two GPM product versions (panels c & e, and d & f, respectively).

The methodology has several key steps. To facilitate the IMERG-GMI error diagnosis, the GR and GPROF-CLIM precipitation products are gridded to IMERG's spatial resolution, and errors are traced from GPROF-CLIM through successive steps of the IMERG algorithm. Quality control procedures are applied to support diagnosis activities, such as restricting the analysis to open ocean regions with high-quality liquid-phase GR retrievals. Finally, a range of statistical measures are applied to diagnose the detection and quantification skills of the GPM products.

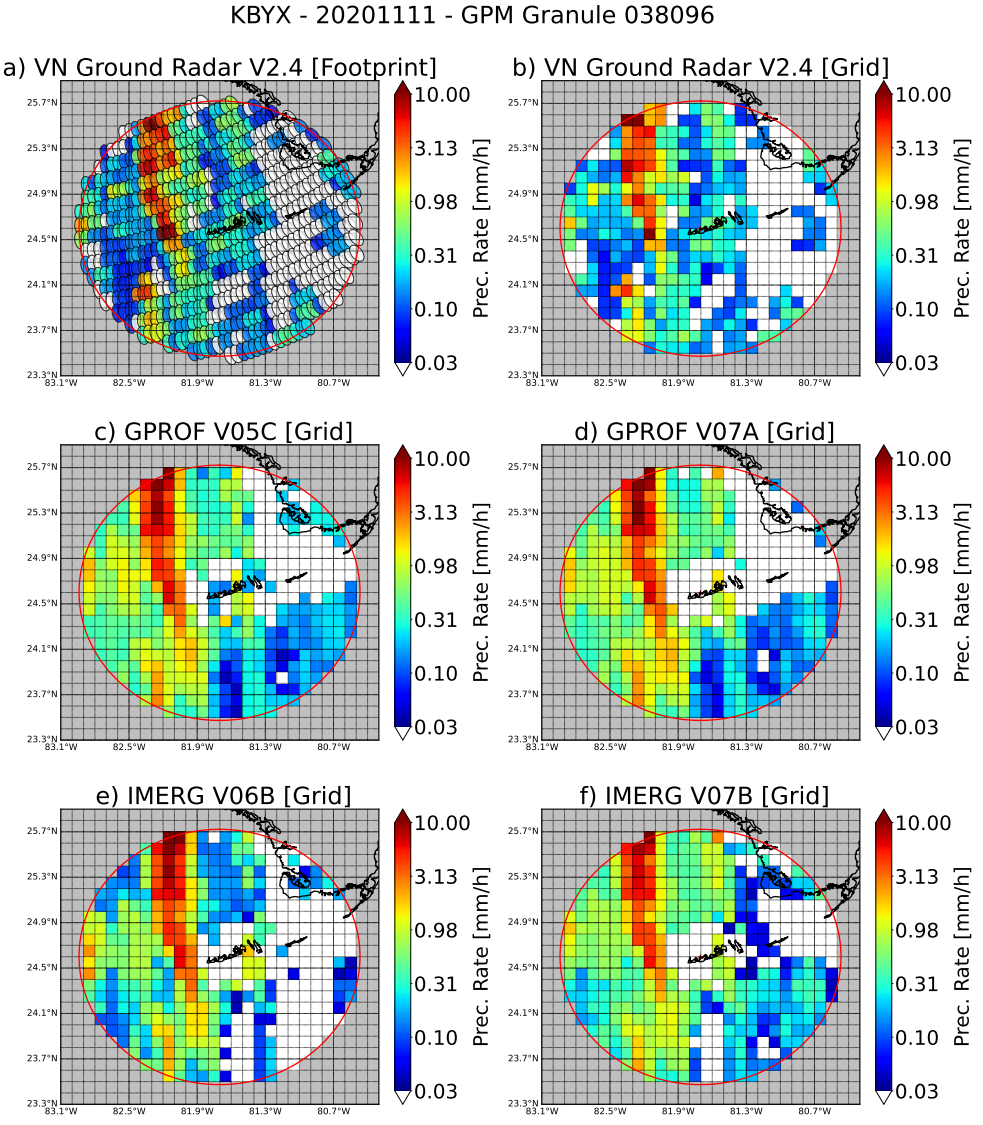

Fig. 3. A case study of precipitation retrievals from Florida's Boca Chica Key GR (KBYX), GPROF-CLIM and IMERG-GMI corresponding to the GPM-CO GMI overpass (granule 38096) on 11 November 2020 at 13:57 UTC. The VN's GR estimates from the lowest elevation scan (start time 13:57:02) are depicted at both a) the GPROF-GMI footprint scale (10.9 km × 18.1 km), and b) on the IMERG 0.1° × 0.1° grid. Gridded GPROF-CLIM c) V05C and d) V07A retrievals (13:56:00-13:56:34), and the respective IMERG-GMI e) V06B and f) V07B retrievals (13:30:00 – 13:59:59) are presented (depicting the first and last steps in the IMERG-GMI V06B and V07B algorithms, respectively; Figure 1). Precipitation rates below 0.03 mm h^{-1} are set to white to signify no rain. The red circle represents 125-km range from the GR.

a. Gridding Process

IMERG's backward gridding technique is used to grid the GR and GPROF-CLIM precipitation estimates at the GPROF-GMI footprint scale to the IMERG $0.1^\circ \times 0.1^\circ$ grid scale (Figure 3a & b). This gridding facilitates error tracing from GPROF-CLIM to IMERG by providing a field not currently available in the IMERG data files: the gridded-but-uncalibrated PMW precipitation rates (Figure 1). Backward gridding, also known as "nearest source to destination", assigns a satellite footprint value to the closest grid box/es on a cylindrical equidistant grid (see Watters et al. 2024 for more details). The gridded GPROF-CLIM precipitation rates are rounded to two decimal places, then rates below 0.03 mm h^{-1} are set to zero (i.e., no-rain); a further V07 gridder criterion is that any GPROF-CLIM V07 footprint flagged as containing no precipitation is also set to zero in the respective grid box/es. In this study, GPROF-CLIM's surface type index is also subject to backward gridding. For the V06 analysis, we do not subject the GR or GPROF-CLIM gridded precipitation rates to the IMERG V06B gridder geolocation offset (Section 2a; Watters et al. 2024), though the subsequent IMERG-GMI V06B variables include the offset as they are output by the IMERG V06B product.

In contrast, other GR geophysical variables, such as HID and GR measurement bin height, are gridded by the fine/average technique (Watters et al. 2024) because it provides a representation of the intra-grid-box spatial distribution (unlike the IMERG backward gridder) by weighting the contribution of multiple nearby GMI-scale footprints. The fine/average gridder assigns a GR variable at the GPROF-GMI footprint scale to the nearest grid box on a finer-resolution $0.025^\circ \times 0.025^\circ$ cylindrical equidistant grid, before mapping the mean/mode of the sixteen fine-scale grid boxes to the encompassing $0.1^\circ \times 0.1^\circ$ grid box; the mode statistic is used for HID and GR measurement bin height.

b. IMERG-GMI Error Tracing

In this analysis, we diagnose IMERG-GMI's oceanic performance by tracing systematic and random errors from the inception of the IMERG algorithm (variable 1: GPROF-CLIM) through to the terminal result (variable 4: Cal; Figures 1 & 3). Only statistical results from the GPROF-CLIM, IMERG-GMI [MW] and IMERG-GMI [Uncal] error tracing variables are shown, as the Uncal and Cal variables are equal over ocean where there is no gauge calibration. Consequently, IMERG-

GMI [Uncal] (variable 3 of 4; Figure 1) can be considered the final output from IMERG V07B for GMI oceanic overpasses; note that rare instances of IR influence introduced by the SHARPEN scheme into IMERG-GMI V07B [Uncal] are removed from this analysis. Alternatively, IMERG-GMI [MW] (variable 2 of 4) can be considered as this final output for IMERG-GMI V06B over ocean since the GMI grid boxes are not subject to PMW propagation or the KF (unlike in V07) and hence MW, Uncal and Cal provide identical statistics. This means that IMERG-GMI V06B errors can only arise from two algorithm procedures, the IMERG V06B geolocation offset and the CORRA-GPCP calibration scheme (Figure 1; GPROF-CLIM $\rightarrow$ MW), whose disaggregated errors have been analyzed by Watters et al. (2024) and hence are not assessed here. Figures 3, 4 & 6 show the final oceanic output when referencing IMERG-GMI.

c. Quality Control Criteria

Several quality control criteria are applied prior to evaluation of the GPM products. Oceanic analysis away from coastlines is ensured by selecting the open-ocean criteria from both GPROF (*surfaceTypeIndex* = 1) and IMERG (*percSurfaceWater* > 75%). Only grid boxes that reside within 75-km of the GR location are analyzed to limit GR range-based effects and ensure surface-based comparisons (Watters et al. 2018); this largely limits the GR observations to <0.66 km above the surface. Furthermore, grid boxes are restricted to those where the top of the GR measurement bin is at least 1 km below the 0°C level to avoid radar reflectivity bright band artifacts.

We assess the performance of GPROF-CLIM and IMERG-GMI in detecting liquid- and mixed-phase precipitation (i.e., distinguishing precipitation occurrence), but then restrict the quantification analysis to liquid-phase precipitation only (i.e., capturing precipitation rate). Including all precipitation types except ice-phase precipitation (due to their exclusion in GR retrieval algorithms) in the detection assessment prevents skewed occurrence values, whilst the quantification assessment is limited to rainfall and drizzle only as radar retrievals are better tuned to liquid-phase hydrometeors (Rauber and Nesbitt 2018). In the quantification analysis, grid boxes are limited to those for which both the GPM and GR products have precipitation rates ≥ 0.03 mm h^{-1} (i.e., the IMERG minimum precipitation rate).

d. Validation Statistics

Validation statistics are determined for each oceanic domain, utilizing the aggregation of quality-controlled grid boxes from each GR within the domain for the respective detection and quantification assessments of the GMI products.

To assess the precipitation detection performance of the GPM GMI products, a set of contingency table values are determined. Hit (h) is the number of grid boxes where both the GMI and GR detected precipitation (i.e., $R_{\mathrm{GMI}} \geq R_{\mathrm{thres.}}$ & $R_{\mathrm{GR}} \geq R_{\mathrm{thres.}}$, where R is precipitation rate and thres. represents threshold). Miss (m) is the number of grid boxes where the GMI did not detect precipitation but the GR did (i.e., $R_{\mathrm{GMI}} < R_{\mathrm{thres.}}$ & $R_{\mathrm{GR}} \geq R_{\mathrm{thres.}}$). Correct rejection ($c$) is the number of grid boxes in which both the GMI and GR did not detect precipitation (i.e., $R_{\mathrm{GMI}} < R_{\mathrm{thres.}}$ & $R_{\mathrm{GR}} < R_{\mathrm{thres.}}$). False alarm ($f$) is the number of grid boxes where the GMI detected precipitation but the GR did not (i.e., $R_{\mathrm{GMI}} \geq R_{\mathrm{thres.}}$ & $R_{\mathrm{GR}} < R_{\mathrm{thres.}}$). In this study, a range of thresholds will be used to examine the detection skill at various intensities.

These contingency table values are used to determine various statistical measures including the probability of detection (POD):

$$\mathrm{POD} = \frac{h}{h+m}, \tag{1}$$

which details the ratio of GR precipitation events that the GMI detects and has an optimal value of 1, and the false alarm ratio (FAR):

$$\mathrm{FAR} = \frac{f}{f+h}, \tag{2}$$

which assesses the ratio of GMI precipitation events for which the GR does not detect precipitation and has an optimal value of 0. Finally, the Heidke Skill Score (HSS; Heidke 1926):

$$\mathrm{HSS} = \frac{2(hc - fm)}{f^2 + m^2 + 2hc + (f+m)(h+c)}, \tag{3}$$

is an equitable performance score which we use to assess the precipitation detection skill of the GMI algorithms, i.e., the HSS quantifies the ability to distinguish between precipitation and no precipitation. The optimal HSS of 1 signifies that the GMI and the reference GR completely align in their detection of precipitation, whilst a score of 0 signifies that the GMI algorithm can distinguish precipitation occurrence no better than random chance when compared to the reference GR. A HSS

above 0.3 represents significant skill in satellite detection of precipitation (Derin et al. 2021). The GR threshold which maximizes the HSS when considering all positive GMI precipitation rates can be defined as the GMI detection threshold (Kirstetter et al. 2015; Watters et al. 2018), because the reference GR is considered to better quantify the GMI detections than the GMI itself. We use this definition to determine the GMI oceanic detection threshold for GPROF-CLIM and IMERG-GMI.

The performance of the GMI products for quantifying oceanic liquid precipitation is assessed with another set of statistical measures. GMI systematic errors are defined by the normalized mean relative bias:

$$\text{Mean Relative Bias } [\%] = \frac{\sum_{i=1}^{N} \Delta R_i}{\sum_{i=1}^{N} R_{\text{GR},i}} \times 100\%, \tag{4}$$

and the normalized mean absolute bias:

$$\text{Mean Absolute Bias } [\%] = \frac{\sum_{i=1}^{N} |\Delta R_i|}{\sum_{i=1}^{N} R_{\text{GR},i}} \times 100\%, \tag{5}$$

where i is the grid box index, N is the sample number of grid boxes, $R_{\text{GMI},i}$ and $R_{\text{GR},i}$ are the precipitation rates for the GMI and GR products at grid box i, respectively, and $\Delta R_i = R_{\text{GMI},i} - R_{\text{GR},i}$. Random errors are defined by the statistic:

$$\text{Random Error } [\%] = \frac{\sum_{i=1}^{N} |\Delta R_i - \overline{\Delta R_i}|}{\sum_{i=1}^{N} R_{\text{GR},i}} \times 100\%, \tag{6}$$

which is a first-order equivalent to the second-order standard deviation statistic, where $\overline{\Delta R_i} = (\sum_{i=1}^{N} \Delta R_i)/N$ and $\overline{R_{\text{GR}}} = (\sum_{i=1}^{N} R_{\text{GR},i})/N$. All error statistics have an optimal value of 0%. Negative mean relative biases express underestimation by the GMI relative to the GR, whilst positive values express overestimation. The linear correlation between the GMI products and the GR is assessed using the Pearson correlation coefficient, which has an optimal value of 1.

4. Results

IMERG-GMI V06B and V07B are assessed relative to the GPM VN GRs for June 2014 – September 2021.

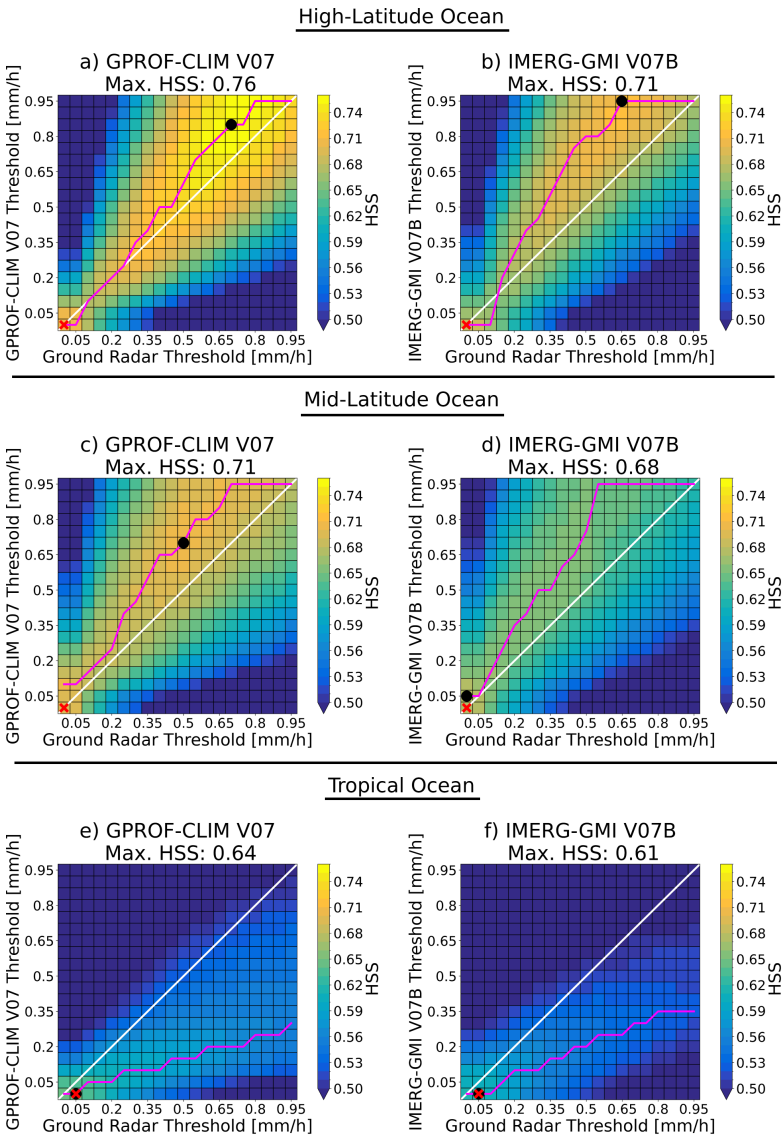

Fig. 4. HSS over high-latitude (a & b), mid-latitude (c & d), and tropical oceans (e & f) as a function of GMI (GPROF-CLIM V07 and IMERG-GMI Final Run V07B) and GR precipitation–no precipitation thresholds. Results are restricted to GMI overpasses when precipitation occurs in the GR vicinity in the period June 2014 – September 2021. The black circle represents the GMI and GR thresholds that give the maximum HSS (i.e., the best agreement between the GMI and the GR when distinguishing precipitation and no precipitation; see plot subtitles), the red cross represents the GMI detection threshold, and the magenta line highlights the GMI threshold that gives the maximum HSS as a function of the GR threshold.

a. Detection Performance Analysis

Figure 4 and Table 2 depict the variation in oceanic precipitation detection performance between GPROF-CLIM, IMERG-GMI [MW] and IMERG-GMI [Uncal]. We focus on the HSS metric as it quantifies GMI detection performance relative to the balance between hits, misses, correct rejections and false alarms, with higher HSS values signifying improved detection capabilities. Two-dimensional HSS histograms can be informative on many aspects of IMERG performance (Derin et al. 2021); for instance, the maximum HSS line (magenta line) in Figure 4 typically resides below the 1:1 line for the tropical ocean and above the 1:1 line for the mid- and high-latitude oceans, signifying that the GMI V07 products tend to underestimate tropical oceanic precipitation and overestimate oceanic precipitation (to a lesser extent) outside of the tropics, respectively (Wolff and Fisher 2009). However, we focus on the satellite detection threshold component of the 2D HSS in this study.

GPROF-CLIM exhibits markedly higher precipitation detection skill relative to IMERG-GMI over all oceanic domains (Figure 4; evident from the maximum HSS), with a tendency for degradation in detection skill across subsequent IMERG algorithm steps (see the POD and HSS trends in Table 2). However, IMERG-GMI V07B better retains the detection performance of the algorithm-input GPROF-CLIM compared to IMERG-GMI V06B (Table 2). Interestingly, the reduction in FAR and POD from GPROF-CLIM to IMERG-GMI suggests that IMERG reduces the precipitation occurrence from the input GPROF-CLIM estimates.

The results also suggest that the oceanic precipitation detection skill of the GMI products improves with latitude. This HSS latitudinal dependency is likely due to the tendency for small-scale fast-evolving isolated convective events over tropical ocean, with spatial scales smaller than the GMI footprints and sparse GPM-CO sampling limiting detectability, and widespread stratiform events over high-latitude ocean, with spatial scales larger than the GMI footprints which enhance detectability.

This HSS analysis allows for a novel assessment of the GMI detection threshold for oceanic precipitation by identifying the GR threshold which maximizes the HSS when all positive GMI precipitation rates are considered (see the bottom row and red cross for each panel in Figure 4; Kirstetter et al. 2015). Figure 5 highlights the variation in the GMI detection threshold when traced through the IMERG V06B & V07B algorithms across various oceanic domains. IMERG-

TABLE 2. Oceanic precipitation detection statistics for IMERG-GMI Final Run and GPROF-CLIM relative to the GPM VN GRs. A precipitation-no precipitation threshold of 0.03 mm h^{-1} is placed on the respective GMI and GR datasets for these results. The period of record is June 2014 – September 2021 when the GPM-CO GMI overpasses precipitating fields close to the GRs. Bold font highlights the best value of a statistical measure within a specific oceanic domain, whilst italic font highlights the respective worst value.

Oceanic Domain	Product	POD	FAR	HSS
High-Latitude	GPROF-CLIM V07	**0.73**	*0.17*	**0.71**
	IMERG-GMI [MW] V07B	0.69	**0.13**	0.70
	IMERG-GMI [Uncal] V07B	0.69	0.16	0.68
	GPROF-CLIM V05	0.68	0.16	0.68
	IMERG-GMI [MW] V06B	*0.63*	**0.13**	*0.66*
	IMERG-GMI [Uncal] V06B	*0.63*	**0.13**	*0.66*
Mid-Latitude	GPROF-CLIM V07	**0.84**	*0.24*	**0.70**
	IMERG-GMI [MW] V07B	0.79	0.20	**0.70**
	IMERG-GMI [Uncal] V07B	0.77	0.21	0.68
	GPROF-CLIM V05	0.81	0.23	0.69
	IMERG-GMI [MW] V06B	*0.63*	**0.15**	*0.62*
	IMERG-GMI [Uncal] V06B	*0.63*	**0.15**	*0.62*
Tropical	GPROF-CLIM V07	0.71	0.21	**0.64**
	IMERG-GMI [MW] V07B	0.70	**0.19**	**0.64**
	IMERG-GMI [Uncal] V07B	0.67	0.21	0.61
	GPROF-CLIM V05	**0.72**	*0.24*	0.63
	IMERG-GMI [MW] V06B	*0.54*	0.22	*0.51*
	IMERG-GMI [Uncal] V06B	*0.54*	0.22	*0.51*

GMI V07B once again improves upon its predecessor V06B by exhibiting lower GMI detection thresholds over the high-latitude and mid-latitude oceans (V07B: 0.03 mm h^{-1} & 0.03 mm h^{-1}, respectively; V06B: 0.10 mm h^{-1} & 0.06 mm h^{-1}, respectively). Over the tropical ocean, both IMERG-GMI versions have the same GMI detection threshold (V07B & V06B: 0.05 mm h^{-1}). In terms of IMERG-GMI error tracing, IMERG-GMI V07B retains the GMI detection threshold of the algorithm input GPROF-CLIM V07 over all oceanic domains when subjecting GPROF-CLIM to CORRA-GPCP calibration and SHARPEN processes. The 0.1°-eastward geolocation error and CORRA-GPCP calibration in IMERG-GMI V06B cause a deterioration in the GMI detection threshold from input GPROF-CLIM V05 over the high-latitude ocean (GPROF-CLIM V05: 0.03 mm h^{-1}; IMERG-GMI [MW] V06B: 0.10 mm h^{-1}) and mid-latitude ocean (GPROF-

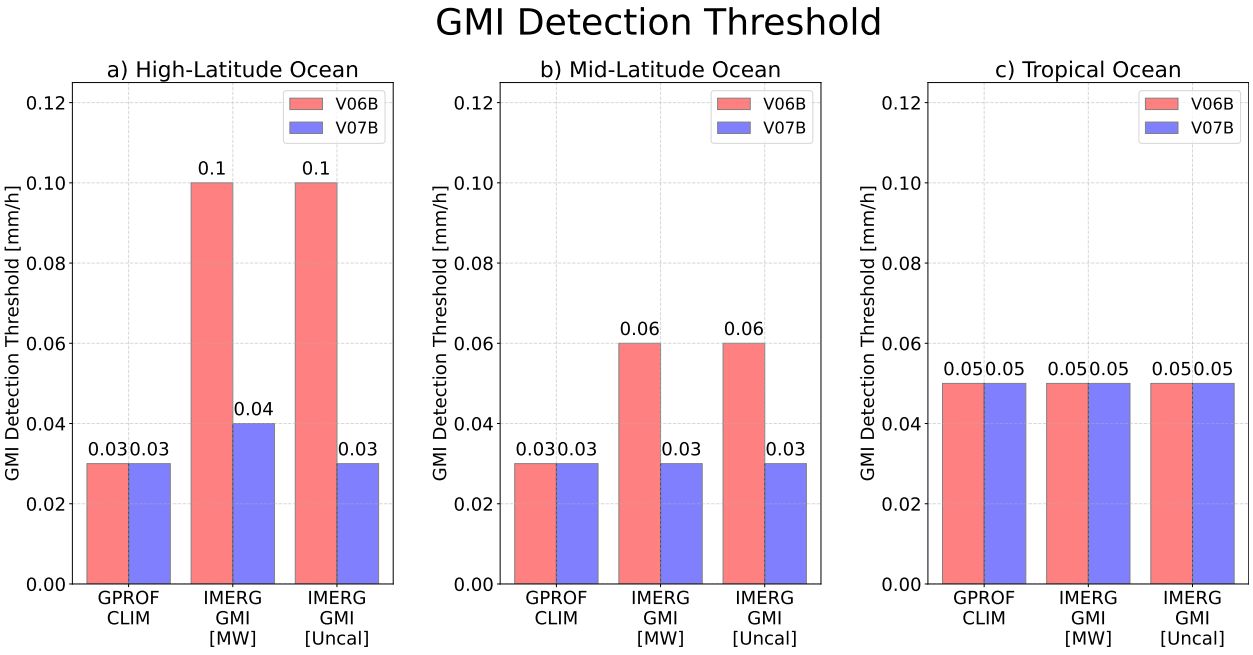

FIG. 5. Bar charts of the GMI detection threshold for subsequent steps in the IMERG V06B and V07B algorithms over the (a) high-latitude ocean, (b) mid-latitude ocean, and (c) tropical ocean. The GMI detection threshold for the first and last step in the IMERG V07B algorithm can be identified by the red cross in Figure 4.

CLIM V05: 0.03 mm h^{-1}; IMERG-GMI [MW] V06B: 0.06 mm h^{-1}). Furthermore, this IMERG-GMI V06B deterioration has a latitudinal dependency, with increasing deterioration at higher latitudes. Another latitudinal dependency is apparent in GPROF-CLIM V07 and IMERG-GMI V07B, such that the GMI can detect lighter precipitation over the high- and mid-latitude oceans (0.03 mm h^{-1}) than over the tropical ocean (0.05 mm h^{-1}). A higher GMI detection threshold over the tropical ocean is likely caused by a tendency for isolated convective events close to the Equator that are not easily detected by the GMI's lower-frequency 18.7-GHz & 36.5-GHz channels (favored for detecting oceanic precipitation; Hou et al. 2014) due to their sub-footprint scale, requiring these events to have higher precipitation rates to be identified by the GMI. Furthermore, these isolated tropical events are often warm rain (Schumacher and Houze 2003; Lau and Wu 2003), which the GMI struggles to detect.

Figure 4 highlights that the precipitation-no precipitation thresholds for the GMI and GR products which provide the maximum HSS (see the black circles) are highly variable between oceanic domains and between the different IMERG-GMI algorithm variables, but the HSS values across

the range of thresholds are typically similar. Consequently, we select a consistent precipitation–no precipitation threshold of 0.03 mm h^{-1} for the subsequent quantitative performance analysis. There are two reasons for selecting this precipitation-no precipitation threshold: 1) this is the IMERG minimum precipitation rate, which ensures that the sample size for the subsequent precipitation-only analysis is maximized; and 2) the detection skill at this threshold remains similar to those which provide the maximum detection skill (i.e., HSS values with a $\leq$0.06 difference).

b. Quantitative Performance Analysis

Figure 6 showcases density scatterplots comparing the rainfall estimates from the GMI V07 products to the VN GRs over various oceanic domains. Only rainfall rates above the selected precipitation-no precipitation threshold of 0.03 mm h^{-1} are considered. Each oceanic domain is well sampled across the analysis period, with all GMI-GR comparisons over high-latitude and tropical oceans having >33,000 samples (Figure 7). The rainfall sample over the mid-latitude ocean is lower, ranging between 10,177 and 13,314 for the GMI products; note that most mid-latitude GRs are located on CONUS coastlines where roughly half of their radar sampling is over land (Figure 2). Interestingly, the sample size reduces with successive steps through the IMERG-GMI V06B & V07B algorithms, suggesting that the CORRA-GPCP calibration process (and SHARPEN scheme in V07 only) can reduce some GPROF-GMI rainfall rates below the IMERG minimum precipitation rate, particularly over the tropical ocean. However, the IMERG-GMI V07B algorithm retains more rainfall events from the input GPROF-CLIM product than its V06B counterpart, as evident from smaller reductions in sample size with each successive IMERG-GMI variable.

The mean relative bias of IMERG-GMI and GPROF-CLIM is latitudinally dependent over ocean (Figures 6 & 8). Specifically, the GMI products overestimate high-latitude oceanic rainfall and underestimate tropical oceanic precipitation relative to the reference GRs, as evident by the quantile-quantile (blue) line generally residing above the 1:1 (black) line in Figure 6 and vice versa, respectively. Furthermore, GPROF-CLIM's mean absolute bias and random error decrease with increasing latitude whilst the correlation with the VN GRs increases (Figures 9–11). Whilst the trend of increasing correlation with increasing latitude translates from GPROF-CLIM to IMERG-GMI, GPROF-CLIM's trend in mean absolute bias and random error does not. The latitudinal dependency on systematic and random errors in GMI products over ocean may be explained

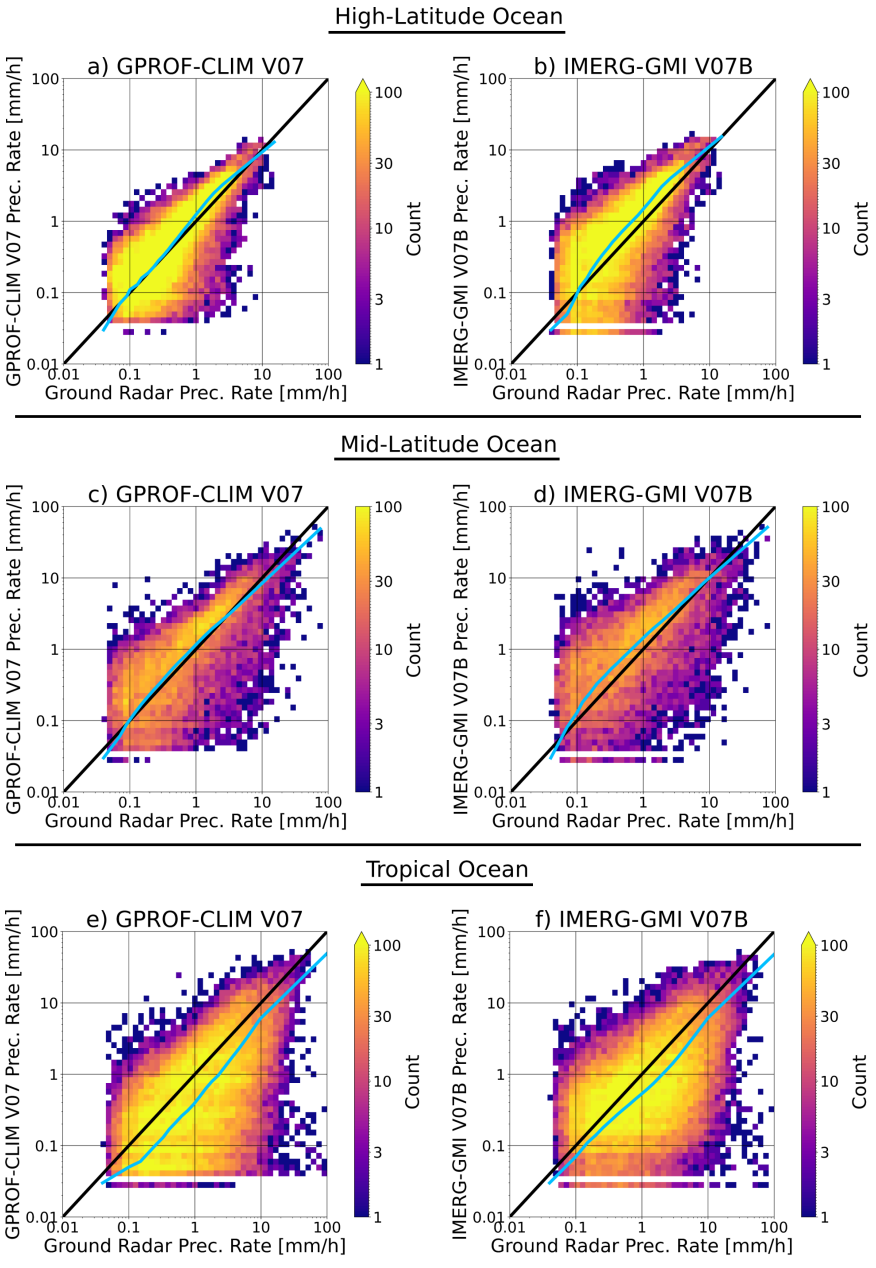

554 FIG. 6. Density scatterplots of gridded rainfall estimates from GPROF-CLIM V07 and IMERG-GMI V07
555 relative to the GPM VN's GRs over high-latitude ocean (a & b, respectively), mid-latitude ocean (c & d,
556 respectively), and tropical ocean (e & f, respectively). Results are restricted to GMI overpasses when precipitation
557 occurs in the GR vicinity in the period June 2014 – September 2021. The quantile-quantile line is blue, and the
558 1:1 line is black.

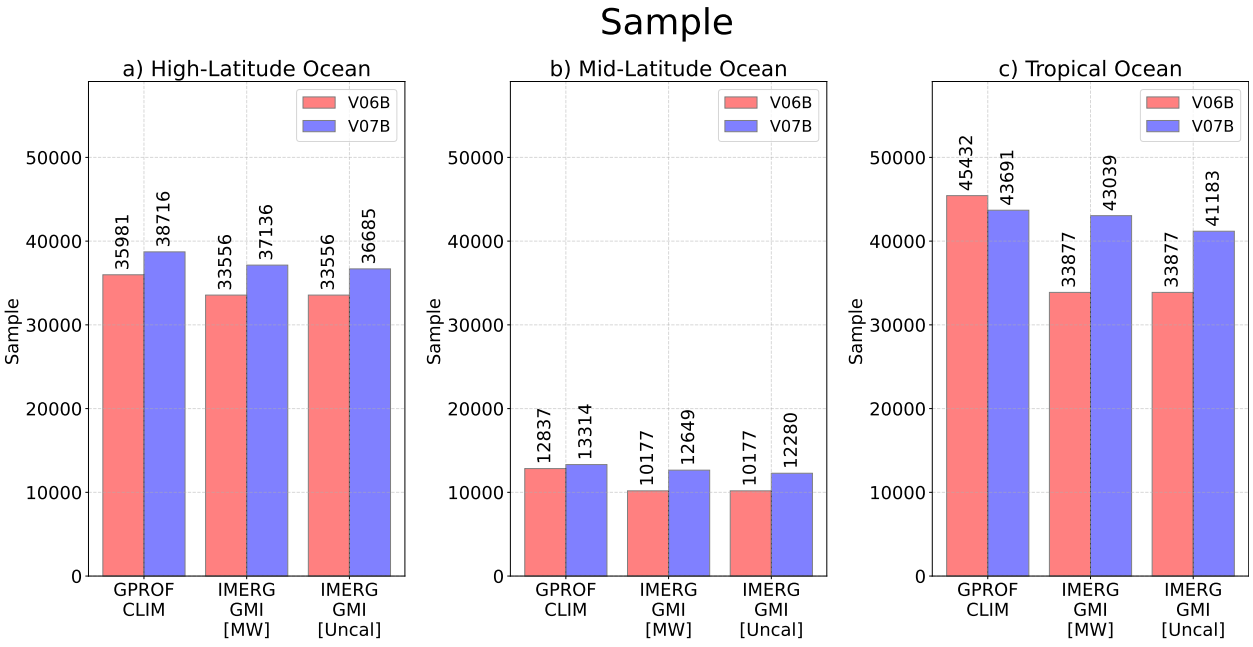

FIG. 7. As in Figure 5, but for rainfall sample.

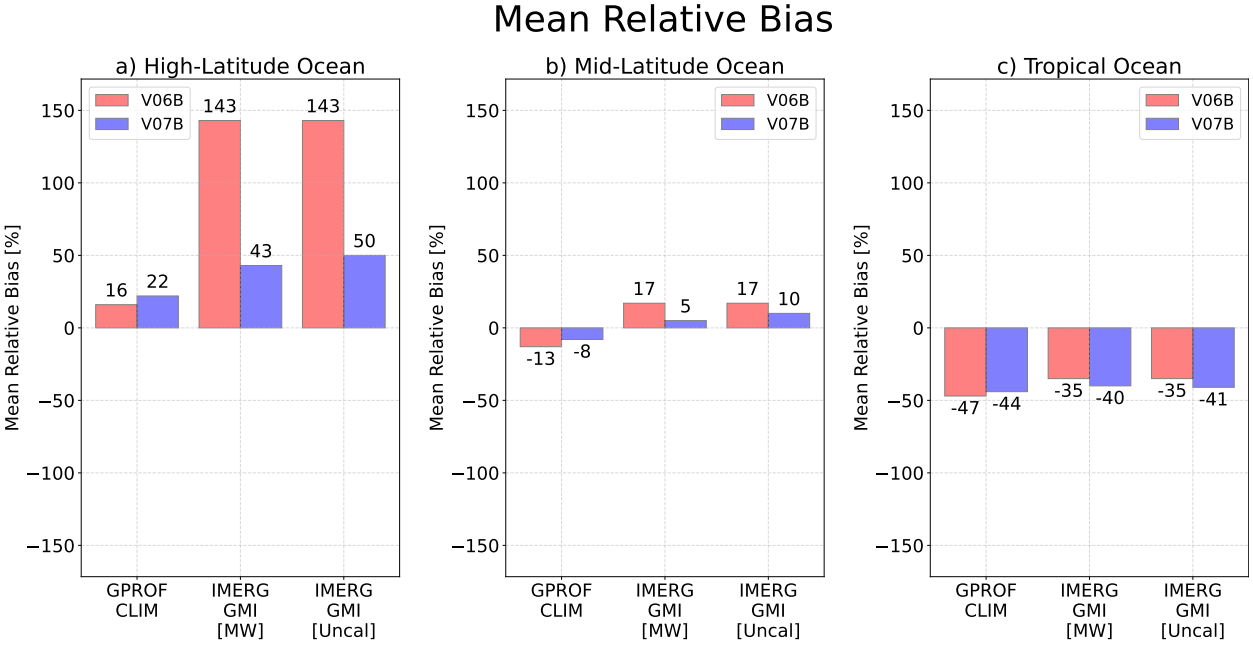

FIG. 8. As in Figure 5, but for mean relative bias.

by the precipitation typology; tropical waters are more susceptible to convective precipitation, which GPROF GMI tends to underestimate with higher variability, whilst high-latitude waters are more susceptible to stratiform precipitation, which GPROF GMI tends to overestimate with lower

variability (Kirstetter et al. 2020; Watters 2021). Furthermore, the GMI's reduced sensitivity to tropical oceanic precipitation (Figure 5), likely caused by a tendency for isolated, oceanic warm rain events close to the Equator, may explain the GMI's underestimation of tropical oceanic precipitation relative to GRs, which are less susceptible to missing warm rain events due to their finer spatial resolution and higher sensitivity compared to the GMI.

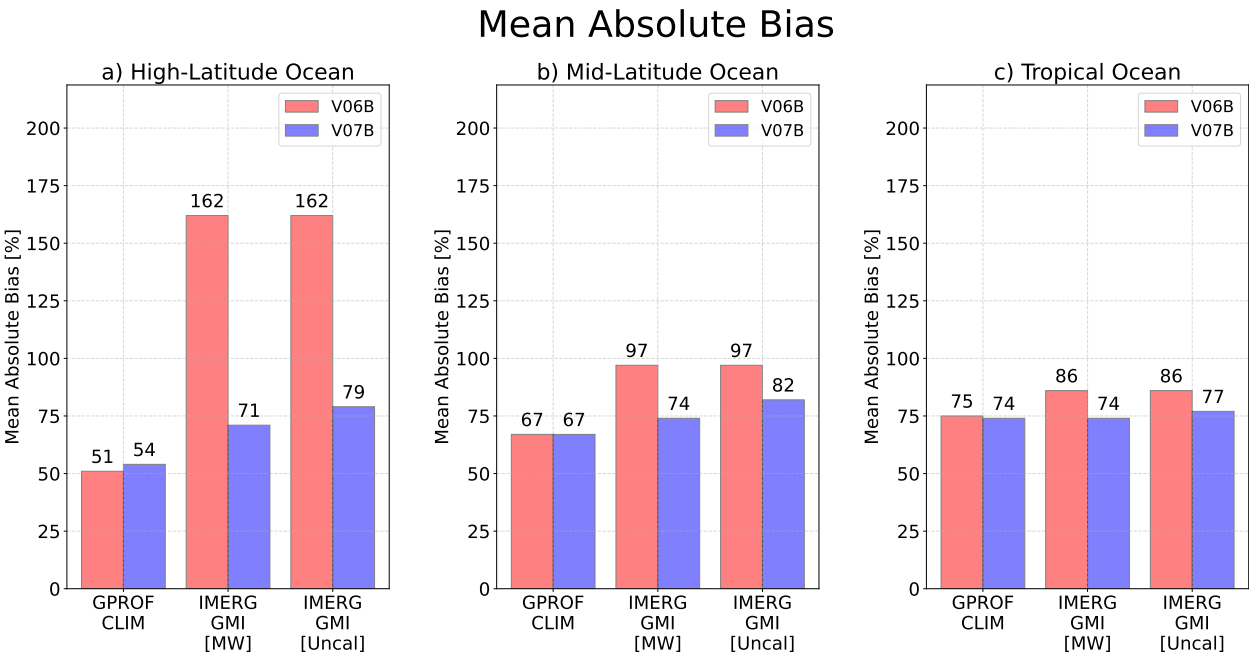

FIG. 9. As in Figure 5, but for mean absolute bias.

Successive IMERG algorithm components tend to reduce its performance in estimating oceanic precipitation rates at GMI overpasses. This is evident from statistical measures such as mean absolute bias, random error and correlation (Figures 9–11), and is particularly prominent over the mid- and high-latitude oceans. However, the CORRA-GPCP calibration applied to GPROF-CLIM in IMERG-GMI V07B does reduce the mean relative bias over tropical and mid-latitude oceans, whilst SHARPEN increases the mean relative biases over all oceanic domains. Whilst IMERG-GMI performance slightly degrades through the algorithm, the IMERG algorithm is designed to optimize measures such as greater consistency amongst constellation sensors rather than mean absolute bias, random error and correlation in pursuit of producing a high-quality multi-satellite precipitation product (Tan et al. 2021). Consequently, some degradation in these metrics is to be expected. In particular, post-processing calibration schemes, such as the CORRA-GPCP calibration applied

to input GPROF-CLIM data, can help to improve systematic errors but result in degradations of random errors and correlations (Ciach et al. 2000; Shen et al. 2024).

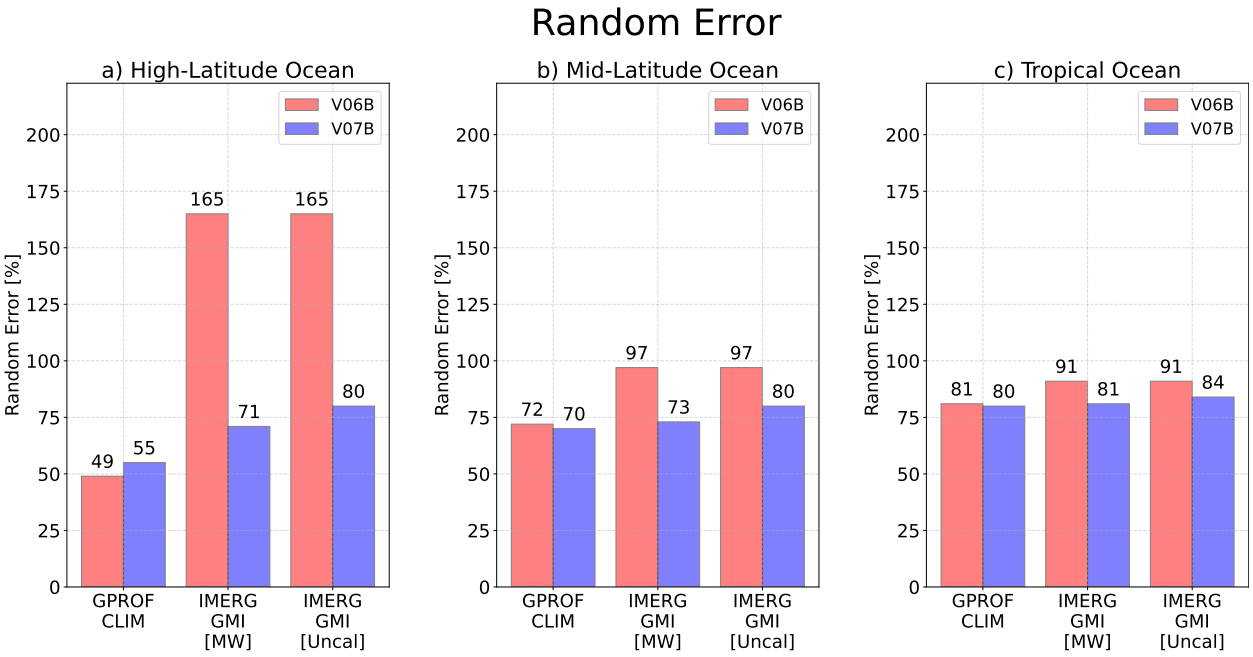

FIG. 10. As in Figure 5, but for random error.

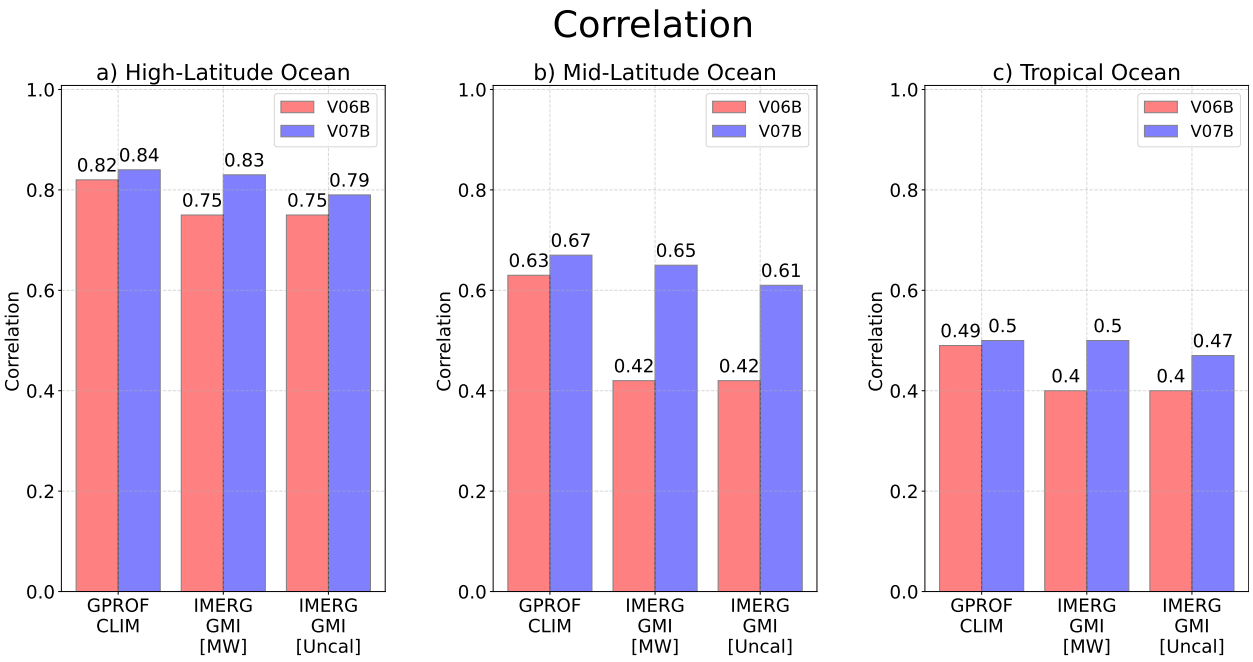

FIG. 11. As in Figure 5, but for correlation.

Over the tropical ocean, the degradation in error metrics from GPROF-CLIM V05 to IMERG V06B is caused by the IMERG V06B 0.1°-eastward gridder offset, because the CORRA-GPCP calibration process has little effect on performance (Watters et al. 2024). With the geolocation error corrected in IMERG V07B, tropical oceanic performance is consistent throughout the algorithm.

Over the high-latitude ocean, the GPCP climatological adjustment in IMERG's CORRA-GPCP calibration scheme drives the increase in overestimating mean relative bias from GPROF-CLIM (V07: +22%; V05: +16%) to IMERG-GMI (V07: +50%; V06: +143%; Watters et al. 2024). A degradation in the mean absolute bias, random error and correlation of IMERG-GMI is also driven by the GPCP climatological adjustment process (Figures 9a, 10a, & 11a, respectively). Notably, IMERG-GMI V07B significantly improves upon the high-latitude oceanic errors of its V06B counterpart, which is likely due to the reduction in GPCP's Alaskan oceanic precipitation rates from V2.3 (used in IMERG V06B) to V3.2 (used in IMERG V07B; see figure 4 of Huffman et al. 2023a).

5. Discussion

This IMERG-GMI error tracing analysis is designed to identify potential improvements at each step of the IMERG algorithm (Figure 1) and provide an update on its performance in the wake of the recent V07B release in January 2024. It is evident that IMERG V07B outperforms IMERG V06B at GMI overpasses in almost all statistical measures including precipitation detection measures, rainfall systematic and random errors, and correlations (Figures 6–11). This improvement between versions appears to be driven by improvements to the CORRA calibration and GPCP climatological adjustment processes which are most impactful over higher-latitude oceans, and the removal of the V06B PMW gridding geolocation error which is particularly important over the tropical ocean (Watters et al. 2024). The importance of these IMERG improvements is highlighted by the minimal statistical differences between GPROF-CLIM GMI V05 & V07. IMERG's PMW calibration scheme is the most impactful in terms of statistical measures and so consideration of further improvements to this algorithm step for future product versions is recommended. The results of this study suggest removing IMERG's GPCP climatological adjustment over high-latitude ocean.

This IMERG-GMI oceanic evaluation contributes to the precipitation research community's drive to better constrain oceanic precipitation and improve our representation of the Earth's water and energy budgets. In particular, this analysis identifies important latitudinal error trends in IMERG-GMI performance. Furthermore, the tendency for GPCP to largely overestimate northern high-latitude oceanic precipitation (as evident from the IMERG-GMI error tracing technique and Watters et al. 2024) is seemingly still prevalent in the latest V3.2 product, although reduced from V2.3. The GPCP algorithm development team may consider how to further reduce this high-latitude overestimation of oceanic precipitation in future algorithm versions (Watters et al. 2024). Whilst a GPCP diagnosis is not possible currently, as the GPM VN is tailored to GPM-CO overpasses only and GPCP does not provide algorithm-step outputs like IMERG at present, this study highlights how evaluating IMERG can support GPCP due to their intertwined nature (Huffman et al. 2023a,c).

GR retrievals are considered a reference in this study, like many others, yet should not be considered as absolutely accurate due to innate radar uncertainties (e.g., calibration, elevated scans, signal attenuation, beam blockage, beam resolution, non-uniform beam filling, etc.), and the errors and uncertainties in the physical algorithms which convert radar measurements to precipitation estimates (Kirstetter et al. 2020; Cifelli et al. 2011). Compared to the preceding study by Watters et al. (2024), we have alleviated some GR issues. In particular, we have reduced range-based effects by reducing the analyzed GR range from 125 km to 75 km, and removed the impact of coastline effects on our open ocean results by introducing the GPROF surface type criteria which categorizes coastal waters. Furthermore, the CSU-HIDRO GR retrievals are now replaced at high-latitudes by the polarimetric Z–R retrievals, which has resulted in a reduction in the apparent GMI biases.

When comparing this analysis to our preceding IMERG-GMI V06B oceanic diagnosis (Watters et al. 2024), there is consistency in the IMERG-GMI V06B high-latitude errors after the addition of a further GR in Nome, AK (PAEC) and stricter quality controls. However, the mean relative bias for IMERG-GMI V06B over the tropical ocean has drastically changed from +12% in the previous study to −35% in this study. This is likely caused by the inclusion of eight additional GRs within the tropical domain (including sites in Brazil, Australia and Florida) and stricter quality control procedures.

This study shows that IMERG-GMI V06B & V07B tend to underestimate tropical oceanic precipitation, which is consistent with Wang et al. (2022), who compared IMERG V05 & V06B

to a single GR around Kwajalein waters at the half-hourly scale, and Wu and Wang (2019), who compared IMERG V05 to buoys spread across the tropical Pacific, Atlantic and Indian Oceans. Other tropical ocean studies found overestimation by IMERG V04A (Prakash et al. 2018) and IMERG V06B (Pradhan and Markonis 2023) when compared against a cluster of hourly buoys, and this was reaffirmed for IMERG V06B relative to monthly Pacific atolls (Bolvin et al. 2021). Our findings may differ from other studies as we assess IMERG at GMI overpasses only, whilst other studies consider all GPM constellation radiometers and IR sensors in their IMERG assessments. Further differences may be driven by varying tropical oceanic precipitation biases with longitude (Wu and Wang 2019; Pradhan and Markonis 2023), and the potential for oceanic biases to flip from underestimates at the half-hourly scale to overestimates at the daily scale (Bytheway et al. 2023). Over the mid-latitude ocean surrounding CONUS, our results agree with the findings of Derin et al. (2022) that IMERG overestimates oceanic precipitation in this region. Whilst Derin et al. (2022) quantify the mean relative bias ranging between +26% and +36% for IMERG V06B, our analysis quantifies lower biases of +17% and +10% for IMERG-GMI V06B & V07B, respectively. As the GMI is the highest-quality sensor input to IMERG, improved performance by IMERG-GMI compared to IMERG, which incorporates many PMW and IR sensors, is to be expected. Several studies have highlighted that IMERG V05 & V06B tend to underestimate precipitation over global oceans using shipborne disdrometers (Khan and Maggioni 2019; Kucera and Klepp 2022) and passive aquatic listeners (Bytheway et al. 2023). When accumulating all GR results, we corroborate that IMERG-GMI V07B also underestimates precipitation across the global oceans (mean relative bias of -16%), though find that IMERG-GMI V06B overestimates global oceanic precipitation (+9%).

A novelty of this study beyond the error tracing technique is the GPM VN's oceanic GR network. To our knowledge, the GPM VN offers the most extensive collection of oceanic GRs under a consistent framework to date. When also factoring in the 7+ years of data from most GRs, the GPM VN's suite of oceanic GRs is primed for further oceanic precipitation validation studies. The main limitation of the GPM VN is the restriction of the GR data to GMI overpasses only, and future updates may consider providing quality-controlled GR data across the entire GPM era to support assessments of other satellite precipitation products. Matchups to other GPM constellation members beyond the GMI would facilitate advanced IMERG error tracing and direct

further IMERG algorithm improvements, establishing a more robust program of record for future spaceborne precipitation observing missions (e.g., Braun et al. 2022).

6. Conclusion

We evaluate how the NASA IMERG Final Run V06B & V07B products perform in detecting and quantifying precipitation across the high-latitude, mid-latitude and tropical oceans at instances of GPM-CO GMI overpasses (a.k.a., IMERG-GMI). This study assesses IMERG-GMI's oceanic performance between June 2014 – September 2021, and restricts the analysis to only GMI overpasses to facilitate an extensive error tracing activity, which is paramount for supporting future algorithm developments. Oceanic IMERG-GMI error tracing is made possible by the GPM VN, which spatially and temporally matches GR precipitation estimates to the footprint scale of the IMERG-input GPROF climate (GPROF-CLIM) GMI product (10.9 km $\times$ 18.1 km) across coastal and island-based GR sites (Figure 2). We then grid these GMI-resolution GR and GPROF-CLIM precipitation estimates to the IMERG grid ($0.1^\circ \times 0.1^\circ$ resolution) and utilize the suite of IMERG outputs to validate IMERG-GMI oceanic precipitation at each successive step in the algorithm (Figure 1). This analysis has been instrumental in assessing the new SHARPEN scheme (Tan et al. 2021) and further updates to the IMERG V07B algorithm.

The key results of this study include:

1. IMERG V07B tends to better detect and quantify oceanic precipitation than its predecessor V06B at GMI overpasses (Table 2, Figures 5 & 8–11). Furthermore, IMERG-GMI V07B tends to better retain the performance of the input GPROF-CLIM product than IMERG-GMI V06B.

2. The GMI detects lighter precipitation over the high- and mid-latitude oceans (≥ 0.03 mm h^{-1}) than the tropical ocean (≥ 0.05 mm h^{-1}) for both GPROF-CLIM V07 & IMERG-GMI V07B (Figure 5). The GMI detection capabilities likely degrade over the tropical ocean due to the tendency for isolated convective events at scales smaller than the GMI's 18.7 GHz channel, whilst precipitation fields outside of the tropics are more widespread and hence more easily detected.

3. The mean relative biases for IMERG-GMI and GPROF-CLIM vary with latitude, from larger underestimation over the tropical ocean, to smaller overestimation/underestimation over the mid-latitude ocean, to larger overestimation over the high-latitude ocean (Figure 8).

4. IMERG-GMI performance in quantifying oceanic precipitation rates tends to degrade with successive algorithm steps, particularly over the mid- and high-latitude oceans. Specifically, statistics such as mean absolute bias, random error and correlation degrade after the CORRA-GPCP calibration scheme is applied to GPROF-CLIM, and after the SHARPEN process is conducted (in V07B only; Figures 9–11). However, the CORRA-GPCP calibration scheme in V07B does reduce the mean relative bias over tropical and mid-latitude oceans (Figure 8). The IMERG algorithm pursues production of a high-quality multi-satellite precipitation product, and consequently optimizes measures other than mean absolute bias, random error and correlation.

5. The removal of the IMERG V06B gridder geolocation offset in IMERG V07B has driven its improved capability in retaining the quantitative performance of the input GPROF-CLIM product (Figures 8–11; Watters et al. 2024).

6. The large systematic and random errors over Alaskan high-latitude waters found in IMERG-GMI V06B have been reduced in IMERG-GMI V07B, likely due to the reduction in GPCP's Alaskan oceanic precipitation rates in the latest V3.2 product (Figures 8–10; Watters et al. 2024). Further improvements to GPCP's overestimating bias over Alaskan waters would support improved IMERG-GMI performance in this oceanic domain.

This IMERG-GMI error tracing analysis is the first to evaluate IMERG V07B and to assess how the V07B upgrades have contributed to improvements over V06B. Error tracing analyses for Level-3 multi-satellite precipitation products are critical for understanding their intrinsic uncertainty and improving our estimation of global precipitation (Roca et al. 2021), and this study highlights the value of directed synergistic efforts between product validation scientists and algorithm development teams. These findings have identified targeted improvements to the IMERG algorithm in preparation of the upcoming V08 algorithm, which is expected to be the final substantive IMERG update in the GPM era.

Future work should utilize this IMERG-GMI error tracing framework to evaluate IMERG performance across global land regions and assess V08 performance when it is released. The GPM VN can support future IMERG-GMI studies; whilst originally used to verify that the GPM mission science requirements were met, the GPM VN will be upgraded from a Level-2 (satellite footprint) system to incorporate a Level-3 (gridded) ground validation product, using the methodology of this study and Watters et al. (2024), as originally intended (Hou et al. 2013; Skofronick-Jackson et al. 2017). This study highlights the value of further GPM VN advancements to include the other GPM constellation members, and for full GPM error tracing through the chain of Level-2 and Level-3 GPM products (DPR $\rightarrow$ CORRA $\rightarrow$ GPROF $\rightarrow$ IMERG).

Acknowledgments. Daniel Watters was supported by an appointment to the NASA Postdoctoral Program at NASA Marshall Space Flight Center, administered by Oak Ridge Associated Universities under contract with NASA. Patrick Gatlin, David Bolvin, George Huffman, Robert Joyce, Eric Nelkin, Jackson Tan and David Wolff were supported by NASA Precipitation Measurement Missions funding (program manager Will McCarty). Pierre Kirstetter was funded by the NASA Global Precipitation Measurement Ground Validation program under Grant 80NSSC21K2045 and the Precipitation Measurement Missions program under Grant 80NSSC19K0681. We thank Christian Kummerow [Colorado State University] for discussions on quality control criteria and GPROF performance. We thank two anonymous reviewers for their helpful comments and recommendations which improved the paper.

Data availability statement. The IMERG V06B & V07B Final Run, GPROF-CLIM V05 & V07, and GPM Validation Network GRtoGPROF V2.4 datasets used in this analysis are freely available from Huffman et al. (2019a), Huffman et al. (2023b), Kummerow (2017), Kummerow (2022), and NASA (2024), respectively. The IMERG land-sea mask is freely available from Olson et al. (2019).

References

Adler, R. F., G. Gu, G. J. Huffman, M. R. Sapiano, and J.-J. Wang, 2020: GPCP and the Global Characteristics of Precipitation. *Satellite Precipitation Measurement*, Springer, 677–697.

Adler, R. F., and Coauthors, 2003: The Version-2 Global Precipitation Climatology Project (GPCP) Monthly Precipitation Analysis (1979–Present). *J. Hydrometeor.*, **4**, 1147–1167, https://doi.org/10.1175/1525-7541(2003)004⟨1147:TVGPCP⟩2.0.CO;2.

Allan, R. P., and Coauthors, 2020: Advances in Understanding Large-Scale Responses of the Water Cycle to Climate Change. *Annals of the New York Academy of Sciences*, **1472 (1)**, 49–75, https://doi.org/10.1111/nyas.14337.

Battaglia, A., K. Mroz, D. Watters, and F. Ardhuin, 2019: GPM-Derived Climatology of Attenuation due to Clouds and Precipitation at Ka-Band. *IEEE Transactions on Geoscience and Remote Sensing*, **58**, 1812–1820, https://doi.org/10.1109/TGRS.2019.2949052.

Battaglia, A., and Coauthors, 2020: Spaceborne Cloud and Precipitation Radars: Status, Challenges, and Ways Forward. *Reviews of Geophysics (Washington, DC: 1985)*, **58 (3)**, https://doi.org/10.1029/2019RG000686.

Beck, H. E., and Coauthors, 2023: High-Resolution (1 km) Köppen-Geiger Maps for 1901–2099 Based on Constrained CMIP6 Projections. *Scientific data*, **10 (1)**, 724, https://doi.org/10.1038/s41597-023-02549-6.

Behrangi, A., and Y. Song, 2020: A New Estimate for Oceanic Precipitation Amount and Distribution using Complementary Precipitation Observations from Space and Comparison with GPCP. *Environmental Research Letters*, **15 (12)**, 124 042, https://doi.org/10.1088/1748-9326/abc6d1.

Behrangi, A., Y. Song, G. J. Huffman, and R. F. Adler, 2024: Comparative Analysis of the Latest Global Oceanic Precipitation Estimates from GPM V07 and GPCP V3.2 Products. *J. Hydrometeor.*, **25 (2)**, 293–309, https://doi.org/10.1175/JHM-D-23-0082.1.

Behrangi, A., G. Stephens, R. F. Adler, G. J. Huffman, B. Lambrigtsen, and M. Lebsock, 2014: An Update on the Oceanic Precipitation Rate and Its Zonal Distribution in Light of Advanced Observations from Space. *J. Climate*, **27 (11)**, 3957–3965, https://doi.org/10.1175/JCLI-D-13-00679.1.

Berg, W., T. L'Ecuyer, and J. M. Haynes, 2010: The Distribution of Rainfall over Oceans from Spaceborne Radars. *J. Appl. Meteor. Climatol.*, **49 (3)**, 535–543, https://doi.org/10.1175/2009JAMC2330.1.

Berg, W., and Coauthors, 2016: Intercalibration of the GPM Microwave Radiometer Constellation. *J. Atmos. Oceanic Technol.*, **33**, 2639–2654, https://doi.org/10.1175/JTECH-D-16-0100.1.

Bolvin, D. T., G. J. Huffman, E. J. Nelkin, and J. Tan, 2021: Comparison of Monthly IMERG Precipitation Estimates with PACRAIN Atoll Observations. *J. Hydrometeor.*, **22**, 1745–1753, https://doi.org/10.1175/JHM-D-20-0202.1.

Braun, S. A., J. Yorks, T. Thorsen, D. Cecil, and D. Kirschbaum, 2022: NASA's Earth System Observatory – Atmosphere Observing System. *IGARSS 2022-2022 IEEE International Geoscience and Remote Sensing Symposium*, IEEE, 7391–7393, https://doi.org/10.1109/IGARSS46834.2022.9884029.

Bringi, V., T. Tang, and V. Chandrasekar, 2004: Evaluation of a New Polarimetrically Based Z–R Relation. *J. Atmos. Oceanic Technol.*, **21 (4)**, 612–623, https://doi.org/10.1175/1520-0426(2004)021⟨0612:EOANPB⟩2.0.CO;2.

Bytheway, J. L., E. Thompson, J. Yang, and H. Chen, 2023: Evaluating Satellite Precipitation Estimates over Oceans using Passive Aquatic Listeners. *Geophys. Res. Lett.*, **50**, e2022GL102 087, https://doi.org/10.1029/2022GL102087.

Ciach, G. J., M. L. Morrissey, and W. F. Krajewski, 2000: Conditional Bias in Radar Rainfall Estimation. *J. Appl. Meteor. Climatol.*, **39 (11)**, 1941–1946, https://doi.org/10.1175/1520-0450(2000)039⟨1941:CBIRRE⟩2.0.CO;2.

Cifelli, R., V. Chandrasekar, S. Lim, P. C. Kennedy, Y. Wang, and S. A. Rutledge, 2011: A New Dual-Polarization Radar Rainfall Algorithm: Application in Colorado Precipitation Events. *J. Atmos. Oceanic Technol.*, **28**, 352–364, https://doi.org/10.1175/2010JTECHA1488.1.

Dai, A., 2024: The Diurnal Cycle from Observations and ERA5 in Precipitation, Clouds, Boundary Layer Height, Buoyancy, and Surface Fluxes. *Climate Dynamics*, 1–30, https://doi.org/10.1007/s00382-024-07182-6.

Dai, A., X. Lin, and K.-L. Hsu, 2007: The Frequency, Intensity, and Diurnal Cycle of Precipitation in Surface and Satellite Observations over Low- and Mid-Latitudes. *Climate Dyn.*, **29 (7-8)**, 727–744, https://doi.org/10.1007/s00382-007-0260-y.

Derin, Y., P.-E. Kirstetter, N. Brauer, J. J. Gourley, and J. Wang, 2022: Evaluation of IMERG Satellite Precipitation over the Land–Coast–Ocean Continuum. Part II: Quantification. *J. Hydrometeor.*, **23**, 1297–1314.

Derin, Y., P.-E. Kirstetter, and J. J. Gourley, 2021: Evaluation of IMERG Satellite Precipitation over the Land–Coast–Ocean Continuum. Part I: Detection. *J. Hydrometeor.*, **22**, 2843–2859, https://doi.org/10.1175/JHM-D-21-0058.1.

Dolan, B., S. A. Rutledge, S. Lim, V. Chandrasekar, and M. Thurai, 2013: A Robust C-band Hydrometeor Identification Algorithm and Application to a Long-Term Polarimetric Radar Dataset. *J. Appl. Meteor. Climatol.*, **52 (9)**, 2162–2186, https://doi.org/10.1175/JAMC-D-12-0275.1.

Ellis, T. D., T. L'Ecuyer, J. M. Haynes, and G. L. Stephens, 2009: How Often Does It Rain over the Global Oceans? The Perspective from CloudSat. *Geophys. Res. Lett.*, **36 (3)**, https://doi.org/10.1029/2008GL036728.

Gatlin, P. N., and Coauthors, 2020: The GPM Validation Network and Evaluation of Satellite-Based Retrievals of the Rain Drop Size Distribution. *Atmosphere*, **11**, 1010, https://doi.org/10.3390/atmos11091010.

Hayden, L., and C. Liu, 2021: Differences in the Diurnal Variation of Precipitation Estimated by Spaceborne Radar, Passive Microwave Radiometer, and IMERG. *Journal of Geophysical Research: Atmospheres*, **126**, e2020JD033 020, https://doi.org/10.1029/2020JD033020.

Hayden, L. J., J. Tan, D. T. Bolvin, and G. J. Huffman, 2023: Variations in the Diurnal Cycle of Precipitation and Its Changes with Distance from Shore over Two Contrasting Regions as Observed by IMERG, ERA5, and Spaceborne Ku Radar. *J. Hydrometeor.*, **24**, 675–689, https://doi.org/10.1175/JHM-D-22-0154.1.

Haynes, J. M., T. S. L'Ecuyer, G. L. Stephens, S. D. Miller, C. Mitrescu, N. B. Wood, and S. Tanelli, 2009: Rainfall Retrieval over the Ocean with Spaceborne W-Band Radar. *Journal of Geophysical Research: Atmospheres*, **114 (D8)**, https://doi.org/10.1029/2008JD009973.

Heidke, P., 1926: Berechnung des Erfolges und der Güte der Windstärkevorhersagen im Sturmwarnungsdienst (Calculation of the Success and Goodness of Wind Strength Forecasts in the Storm Warning Service). *Geografiska Annaler*, **8 (4)**, 301–349, https://doi.org/10.1080/20014422.1926.11881138.

Helsel, D. R., and T. A. Cohn, 1988: Estimation of Descriptive Statistics for Multiply Censored Water Quality Data. *Water Resources Research*, **24 (12)**, 1997–2004, https://doi.org/10.1029/WR024i012p01997.

Hersbach, H., and Coauthors, 2020: The ERA5 Global Reanalysis. *Quart. J. Roy. Meteor. Soc.*, **146 (730)**, 1999–2049, https://doi.org/10.1002/qj.3803.

Hou, A. Y., G. Skofronick-Jackson, E. F. Stocker, W. A. Petersen, J. Kaye, and R. Kakar, 2013: Global Precipitation Measurement (GPM) Science Implementation Plan.

Tech. rep., NASA. Accessed March 4 2024, https://gpm.nasa.gov/resources/documents/gpm-science-implementation-plan.

Hou, A. Y., and Coauthors, 2014: The Global Precipitation Measurement Mission. *Bull. Amer. Meteor. Soc.*, **95**, 701–722, https://doi.org/10.1175/BAMS-D-13-00164.1.

Huffman, G. J., R. F. Adler, A. Behrangi, D. T. Bolvin, E. J. Nelkin, G. Gu, and M. R. Ehsani, 2023a: The New Version 3.2 Global Precipitation Climatology Project (GPCP) Monthly and Daily Precipitation Products. *J. Climate*, **36 (21)**, 7635–7655, https://doi.org/10.1175/JCLI-D-23-0123.1.

Huffman, G. J., D. T. Bolvin, E. J. Nelkin, E. F. Stocker, and J. Tan, 2020a: IMERG V06 Release Notes. Tech. rep., NASA. Accessed 16 October 2020, https://gpm.nasa.gov/sites/default/files/2020-10/IMERG_V06_release_notes_201006_0.pdf.

Huffman, G. J., E. Stocker, D. Bolvin, E. Nelkin, and J. Tan, 2019a: GPM IMERG Final Precipitation L3 Half Hourly 0.1 Degree x 0.1 Degree, Version 6B. Greenbelt, MD, Goddard Earth Sciences Data and Information Services Center (GES DISC). Subset used: June 2014 – September 2021, accessed 13 March 2023, https://doi.org/10.5067/GPM/IMERG/3B-HH/06.

Huffman, G. J., E. Stocker, D. Bolvin, E. Nelkin, J. Tan, and R. Joyce, 2023b: GPM IMERG Final Precipitation L3 Half Hourly 0.1 Degree x 0.1 Degree, Version 7B. Greenbelt, MD, Goddard Earth Sciences Data and Information Services Center (GES DISC). Subset used: June 2014 – September 2021, accessed 22 January 2024, https://doi.org/10.5067/GPM/IMERG/3B-HH/07.

Huffman, G. J., and Coauthors, 2019b: NASA Global Precipitation Measurement (GPM) Integrated Multi-satellitE Retrievals for GPM (IMERG) – Algorithm Theoretical Basis Document – Version 6. Tech. rep., NASA, 38 pp. Accessed 24 October 2020, https://pmm.nasa.gov/sites/default/files/document_files/IMERG_ATBD_V06.pdf.

Huffman, G. J., and Coauthors, 2020b: Integrated Multi-satellite Retrievals for the Global Precipitation Measurement (GPM) Mission (IMERG). *Satellite Precipitation Measurement*, Springer, 343–353, https://doi.org/10.1007/978-3-030-24568-9_19.

Huffman, G. J., and Coauthors, 2023c: NASA Global Precipitation Measurement (GPM) Integrated Multi-satellitE Retrievals for GPM (IMERG) – Algorithm Theoretical Basis Document – Version

7. Tech. rep., NASA, 52 pp. Accessed 1 March 2024, https://gpm.nasa.gov/resources/documents/imerg-v07-atbd.

Huffman, G. J., and Coauthors, 2024: IMERG V07 Release Notes. Tech. rep., NASA. Accessed 28 May 2024, https://gpm.nasa.gov/sites/default/files/2024-02/IMERG_V07_ReleaseNotes_240221.pdf.

Iguchi, T., and Coauthors, 2018: GPM/DPR Level-2 Algorithm Theoretical Basis Document. Tech. rep., NASA. Accessed 7 October 2020, https://pps.gsfc.nasa.gov/Documents/ATBD_DPR_201811_with_Appendix3b.pdf.

Joyce, R. J., J. E. Janowiak, P. A. Arkin, and P. Xie, 2004: CMORPH: A Method that Produces Global Precipitation Estimates from Passive Microwave and Infrared Data at High Spatial and Temporal Resolution. *J. Hydrometeor.*, **5 (3)**, 487–503, https://doi.org/10.1175/1525-7541(2004)005⟨0487:CAMTPG⟩2.0.CO;2.

Khan, S., and V. Maggioni, 2019: Assessment of Level-3 Gridded Global Precipitation Mission (GPM) Products over Oceans. *Remote Sensing*, **11**, 255, https://doi.org/10.3390/rs11030255.

Kidd, C., Y. N. Takayabu, G. M. Skofronick-Jackson, G. J. Huffman, S. A. Braun, T. Kubota, and F. J. Turk, 2020: The Global Precipitation Measurement (GPM) Mission. *Satellite Precipitation Measurement*, Springer, 3–23, https://doi.org/10.1007/978-3-030-24568-9_1.

Kirschbaum, D. B., and Coauthors, 2017: NASA's Remotely Sensed Precipitation: A Reservoir for Applications Users. *Bull. Amer. Meteor. Soc.*, **98**, 1169–1184.

Kirstetter, P.-E., Y. Hong, J. Gourley, M. Schwaller, W. Petersen, and Q. Cao, 2015: Impact of Sub-Pixel Rainfall Variability on Spaceborne Precipitation Estimation: Evaluating the TRMM 2A25 Product. *Quart. J. Roy. Meteor. Soc.*, **141 (688)**, 953–966, https://doi.org/10.1002/qj.2416.

Kirstetter, P.-E., Y. Hong, J. J. Gourley, Q. Cao, M. Schwaller, and W. Petersen, 2014: Research Framework to Bridge from the Global Precipitation Measurement Mission Core Satellite to the Constellation Sensors using Ground-Radar-Based National Mosaic QPE. *Remote Sensing of the Terrestrial Water Cycle*, 61–79, https://doi.org/10.1002/9781118872086.ch4.

Kirstetter, P.-E., N. Karbalaee, K. Hsu, and Y. Hong, 2018: Probabilistic Precipitation Rate Estimates with Space-Based Infrared Sensors. *Quart. J. Roy. Meteor. Soc.*, **144**, 191–205, https://doi.org/10.1002/qj.3243.

Kirstetter, P.-E., W. A. Petersen, C. D. Kummerow, and D. B. Wolff, 2020: Integrated Multi-satellite Evaluation for the Global Precipitation Measurement: Impact of Precipitation Types on Spaceborne Precipitation Estimation. *Satellite Precipitation Measurement*, Springer, 583–608, https://doi.org/10.1007/978-3-030-35798-6_7.

Kirstetter, P.-E., and Coauthors, 2012: Toward a Framework for Systematic Error Modeling of Spaceborne Precipitation Radar with NOAA/NSSL Ground Radar–Based National Mosaic QPE. *J. Hydrometeor.*, **13 (4)**, 1285–1300, https://doi.org/10.1175/JHM-D-11-0139.1.

Kubota, T., and Coauthors, 2020: Global Satellite Mapping of Precipitation (GSMaP) Products in the GPM Era. *Satellite Precipitation Measurement: Volume 1*, 355–373.

Kucera, P. A., and C. Klepp, 2022: Evaluation of High-Resolution Satellite Precipitation over the Global Oceans. *Precipitation Science*, Elsevier, 305–332, https://doi.org/10.1016/B978-0-12-822973-6.00008-1.

Kummerow, C., 2017: GPM GMI (GPROF) Climate-based Radiometer Precipitation Profiling, Version 5. Greenbelt, MD, Goddard Earth Sciences Data and Information Services Center (GES DISC). Subset used: June 2014 – September 2021, accessed 13 March 2023, https://arthurhouhttps.pps.eosdis.nasa.gov/gpmallversions/V05/YYYY/MM/DD/gprof.

Kummerow, C., 2022: GPM GMI (GPROF) Radiometer Precipitation Profiling L2A 1.5 hours 13 km, Version 7. Greenbelt, MD, Goddard Earth Sciences Data and Information Services Center (GES DISC). Subset used: June 2014 – September 2021, accessed 22 January 2024, https://doi.org/10.5067/GPM/GMI/GPM/GPROF/2A/07.

Kummerow, C., W. Barnes, T. Kozu, J. Shiue, and J. Simpson, 1998: The Tropical Rainfall Measuring Mission (TRMM) Sensor Package. *J. Atmos. Oceanic Technol.*, **15**, 809–817, https://doi.org/10.1175/1520-0426(1998)015⟨0809:TTRMMT⟩2.0.CO;2.

Kummerow, C. D., D. L. Randel, M. Kulie, N.-Y. Wang, R. Ferraro, S. Joseph Munchak, and V. Petkovic, 2015: The Evolution of the Goddard Profiling Algorithm to a Fully

Parametric Scheme. *J. Atmos. Oceanic Technol.*, **32**, 2265–2280, https://doi.org/10.1175/JTECH-D-15-0039.1.

Lau, K., and H. Wu, 2003: Warm Rain Processes over Tropical Oceans and Climate Implications. *Geophys. Res. Lett.*, **30 (24)**, https://doi.org/10.1029/2003GL018567.

Levizzani, V., C. Kidd, D. B. Kirschbaum, C. D. Kummerow, K. Nakamura, and F. J. Turk, 2020a: *Satellite Precipitation Measurement: Volume 1*. Springer, https://doi.org/10.1007/978-3-030-24568-9.

Levizzani, V., C. Kidd, D. B. Kirschbaum, C. D. Kummerow, K. Nakamura, and F. J. Turk, 2020b: *Satellite Precipitation Measurement: Volume 2*. Springer, https://doi.org/10.1007/978-3-030-35798-6.

Li, Z., E. J. Thompson, A. Behrangi, H. Chen, and J. Yang, 2023: Performance of GPCP Daily Products over Oceans: Evaluation Using Passive Aquatic Listeners. *Geophys. Res. Lett.*, **50 (11)**, e2023GL104 310, https://doi.org/10.1029/2023GL104310.

L'Ecuyer, T. S., and Coauthors, 2015: The Observed State of the Energy Budget in the Early Twenty-First Century. *J. Climate*, **28 (21)**, 8319–8346, https://doi.org/10.1175/JCLI-D-14-00556.1.

Mahmoud, M. T., S. A. Mohammed, M. A. Hamouda, M. Dal Maso, and M. M. Mohamed, 2021: Performance of the IMERG Precipitation Products over High-Latitudes Region of Finland. *Remote Sensing*, **13**, 2073, https://doi.org/10.3390/rs13112073.

Montoya Duque, E., Y. Huang, P. May, and S. Siems, 2023: An Evaluation of IMERG and ERA5 Quantitative Precipitation Estimates over the Southern Ocean Using Shipborne Observations. *J. Appl. Meteor. Climatol.*, **62 (11)**, 1479–1495, https://doi.org/10.1175/JAMC-D-23-0039.1.

NASA, 2015: Validation Network Data Product User's Guide: Volume 2 – GPM Data Products. Tech. rep., NASA. Accessed 17 May 2023, https://gpm.nasa.gov/sites/default/files/document_files/Val_Network_Users_Guide_Vol_2_Nov2015.pdf.

NASA, 2022: GPROF2021 Version 1 - Algorithm Theoretical Basis Document. Tech. rep., NASA. Accessed 27 May 2024, https://gpm.nasa.gov/sites/default/files/2022-06/ATBD_GPM_V7_GPROF.pdf.

NASA, 2024: GPM Validation Network V2.4 GRtoGPROF Data. NASA Marshall Space Flight Center. Subset used: June 2014 – September 2021, accessed 11 January 2024, https://pmm-gv.gsfc.nasa.gov/pub/gpm-validation/data/gpmgv/netcdf/geo_match/GPM/GMI/2AGPROF/V07A/2_4/.

Nguyen, P., and Coauthors, 2020: PERSIANN Dynamic Infrared–Rain Rate (PDIR-Now): A Near-Real-Time, Quasi-Global Satellite Precipitation Dataset. *J. Hydrometeor.*, **21 (12)**, 2893–2906, https://doi.org/10.1175/JHM-D-20-0177.1.

O, S., and P. Kirstetter, 2018: Evaluation of Diurnal Variation of GPM IMERG-derived Summer Precipitation over the Contiguous US using MRMS Data. *Quart. J. Roy. Meteor. Soc.*, **144**, 270–281, https://doi.org/10.1002/qj.3218.

Olson, B., D. Bolvin, and G. Huffman, 2019: Land/Sea Static Mask Relevant to IMERG Precipitation 0.1x0.1 Degree, Version 2. Greenbelt, MD, Goddard Earth Sciences Data and Information Services Center (GES DISC). Accessed 21 February 2022, https://doi.org/10.5067/6P5EM1HPR3VD.

Olson, W. S., 2022: GPM Combined Radar-Radiometer Precipitation Algorithm Theoretical Basis Document (Version 7). Tech. rep., NASA. Accessed 27 May 2024, https://gpm.nasa.gov/sites/default/files/2023-01/Combined_algorithm_ATBD.V07_0.pdf.

Petersen, W. A., P.-E. Kirstetter, J. Wang, D. B. Wolff, and A. Tokay, 2020: The GPM Ground Validation Program. *Satellite Precipitation Measurement*, Springer, 471–502.

Petty, G. W., 1997: An Intercomparison of Oceanic Precipitation Frequencies from 10 Special Sensor Microwave/Imager Rain Rate Algorithms and Shipboard Present Weather Reports. *Journal of Geophysical Research: Atmospheres*, **102 (D2)**, 1757–1777, https://doi.org/10.1029/96JD03000.

Pfreundschuh, S., C. Guilloteau, P. J. Brown, C. D. Kummerow, and P. Eriksson, 2024: GPROF V7 and Beyond: Assessment of Current and Potential Future Versions of the GPROF Passive Microwave Precipitation Retrievals against Ground Radar Measurements over the Continental U.S. and the Pacific Ocean. *Atmospheric Measurement Techniques*, **17 (2)**, 515–538, https://doi.org/10.5194/amt-17-515-2024.

Pippitt, J., D. Wolff, W. Petersen, and D. Marks, 2015: Data and Operational Processing for NASA's GPM Ground Validation Program. 37th Conference on Radar Meteorology, Norman, OK, Amer. Meteor. Soc., 111.

Portier, A., D. Kirschbaum, M. Gebremichael, E. Kemp, S. Kumar, I. Llabres, E. Snodgrass, and J. Wegiel, 2023: NASA's Global Precipitation Measurement Mission: Leveraging Stakeholder Engagement & Applications Activities to Inform Decision-Making. *Remote Sensing Applications: Society and Environment*, **29**, 100 853, https://doi.org/10.1016/j.rsase.2022.100853.

Pradhan, R. K., and Y. Markonis, 2023: Performance Evaluation of GPM IMERG Precipitation Products over the Tropical Oceans Using Buoys. *J. Hydrometeor.*, **24 (10)**, 1755–1770, https://doi.org/10.1175/JHM-D-22-0216.1.

Prakash, S., M. Ramesh Kumar, S. Mathew, and R. Venkatesan, 2018: How Accurate are Satellite Estimates of Precipitation over the North Indian Ocean? *Theoretical and Applied Climatology*, **134**, 467–475, https://doi.org/10.1007/s00704-017-2287-2.

Ramadhan, R., M. Marzuki, W. Suryanto, S. Sholihun, H. Yusnaini, and R. Muharsyah, 2024: Validating IMERG Data for Diurnal Rainfall Analysis across the Indonesian Maritime Continent using Gauge Observations. *Remote Sensing Applications: Society and Environment*, **34**, 101 186, https://doi.org/10.1016/j.rsase.2024.101186.

Randel, D. L., and Coauthors, 2020: The Goddard Profiling (GPROF) Precipitation Retrieval Algorithm. *Satellite Precipitation Measurement*, Springer, 141–152, https://doi.org/10.1007/978-3-030-24568-9_8.

Rauber, R. M., and S. W. Nesbitt, 2018: *Radar Meteorology: A First Course*. John Wiley & Sons.

Roca, R., and Coauthors, 2021: The Joint IPWG/GEWEX Precipitation Assessment. Accessed 6 January 2025, https://www.wcrp-climate.org/WCRP-publications/2021/Joint_IPWG-GEWEX_Precipitation_Assessment_web.pdf.

Schneider, U., A. Becker, P. Finger, A. Meyer-Christoffer, M. Ziese, and B. Rudolf, 2014: GPCC's New Land Surface Precipitation Climatology based on Quality-Controlled In Situ Data and its Role in Quantifying the Global Water Cycle. *Theoretical and Applied Climatology*, **115**, 15–40, https://doi.org/10.1007/s00704-013-0860-x.

Schumacher, C., and R. A. Houze, 2003: The TRMM Precipitation Radar's View of Shallow, Isolated Rain. *J. Appl. Meteor. Climatol.*, **42 (10)**, 1519–1524, https://doi.org/10.1175/1520-0450(2003)042⟨1519:TTPRVO⟩2.0.CO;2.

Schwaller, M. R., and K. R. Morris, 2011: A Ground Validation Network for the Global Precipitation Measurement Mission. *J. Atmos. Oceanic Technol.*, **28**, 301–319, https://doi.org/10.1175/2010JTECHA1403.1.

Shen, Z., B. Yong, and H. Wu, 2024: Which Error Components in TRMM-Based Multisatellite Precipitation Estimates Reduce over Chinese Mainland after Official Bias Adjustments: Systematic or Random? *J. Hydrometeor.*, **25 (4)**, 601–617, https://doi.org/10.1175/JHM-D-23-0172.1.

Simpson, J., C. Kummerow, W.-K. Tao, and R. F. Adler, 1996: On the Tropical Rainfall Measuring Mission (TRMM). *Meteorology and Atmospheric Physics*, **60**, 19–36, https://doi.org/10.1007/BF01029783.

Skofronick-Jackson, G., D. Kirschbaum, W. Petersen, G. Huffman, C. Kidd, E. Stocker, and R. Kakar, 2018: The Global Precipitation Measurement (GPM) Mission's Scientific Achievements and Societal Contributions: Reviewing Four Years of Advanced Rain and Snow Observations. *Quart. J. Roy. Meteor. Soc.*, https://doi.org/10.1002/qj.3313.

Skofronick-Jackson, G., and Coauthors, 2017: The Global Precipitation Measurement (GPM) Mission for Science and Society. *Bull. Amer. Meteor. Soc.*, **98**, 1679–1695, https://doi.org/10.1175/BAMS-D-15-00306.1.

Stephens, G. L., and Coauthors, 2012: An Update on Earth's Energy Balance in Light of the Latest Global Observations. *Nature Geoscience*, **5 (10)**, 691–696, https://doi.org/10.1038/ngeo1580.

Tan, J., G. J. Huffman, D. T. Bolvin, and E. J. Nelkin, 2019: Diurnal Cycle of IMERG V06 Precipitation. *Geophys. Res. Lett.*, **46**, 13 584–13 592, https://doi.org/10.1029/2019GL085395.

Tan, J., G. J. Huffman, D. T. Bolvin, E. J. Nelkin, and M. Rajagopal, 2021: SHARPEN: A Scheme to Restore the Distribution of Averaged Precipitation Fields. *J. Hydrometeor.*, **22**, 2105–2116, https://doi.org/10.1175/JHM-D-20-0225.1.

Tapiador, F., and Coauthors, 2017: Global Precipitation Measurements for Validating Climate Models. *Atmospheric Research*, **197**, 1–20, https://doi.org/10.1016/j.atmosres.2017.06.021.

Trenberth, K. E., L. Smith, T. Qian, A. Dai, and J. Fasullo, 2007: Estimates of the Global Water Budget and its Annual Cycle using Observational and Model Data. *J. Hydrometeor.*, **8**, 758–769, https://doi.org/10.1175/JHM600.1.

Ulbrich, C. W., and D. Atlas, 1998: Rainfall Microphysics and Radar Properties: Analysis Methods for Drop Size Spectra. *J. Appl. Meteor. Climatol.*, **37**, 912–923, https://doi.org/10.1175/1520-0450(1998)037⟨0912:RMARPA⟩2.0.CO;2.

Wang, J., W. A. Petersen, D. B. Wolff, and G.-H. Ryu, 2020: Evaluation of GPM IMERG Products over South Korea. *IGARSS 2020-2020 IEEE International Geoscience and Remote Sensing Symposium*, IEEE, 5356–5359, https://doi.org/10.1109/IGARSS39084.2020.9323244.

Wang, J., D. B. Wolff, J. Tan, D. A. Marks, J. L. Pippitt, and G. J. Huffman, 2022: Validation of IMERG Oceanic Precipitation over Kwajalein. *Remote Sensing*, **14**, 3753, https://doi.org/10.3390/rs14153753.

Warren, R. A., A. Protat, S. T. Siems, H. A. Ramsay, V. Louf, M. J. Manton, and T. A. Kane, 2018: Calibrating Ground-Based Radars against TRMM and GPM. *J. Atmos. Oceanic Technol.*, **35 (2)**, 323–346, https://doi.org/10.1175/JTECH-D-17-0128.1.

Watters, D., and A. Battaglia, 2019: The Summertime Diurnal Cycle of Precipitation Derived from IMERG. *Remote Sensing*, **11**, 1781, https://doi.org/10.3390/rs11151781.

Watters, D., and A. Battaglia, 2021a: The NASA-JAXA Global Precipitation Measurement Mission – Part I: New Frontiers in Precipitation. *Weather*, **76**, 41–44, https://doi.org/10.1002/wea.3865.

Watters, D., and A. Battaglia, 2021b: The NASA-JAXA Global Precipitation Measurement Mission – Part II: New Frontiers in Precipitation Science. *Weather*, **76**, 52–56, https://doi.org/10.1002/wea.3869.

Watters, D., A. Battaglia, and R. P. Allan, 2021: The Diurnal Cycle of Precipitation According to Multiple Decades of Global Satellite Observations, Three CMIP6 Models, and the ECMWF Reanalysis. *J. Climate*, **34**, 5063–5080, https://doi.org/10.1175/JCLI-D-20-0966.1.

Watters, D., A. Battaglia, K. Mroz, and F. Tridon, 2018: Validation of the GPM Version-5 Surface Rainfall Products over Great Britain and Ireland. *J. Hydrometeor.*, **19 (10)**, 1617–1636, https://doi.org/10.1175/JHM-D-18-0051.1, https://doi.org/10.1175/JHM-D-18-0051.1.

Watters, D. C., 2021: The Global Precipitation Measurement Mission: Product Validation and Model Evaluation Studies. Ph.D. thesis, University of Leicester, https://doi.org/10.25392/leicester.data.17099396.v1.

Watters, D. C., and Coauthors, 2024: Oceanic Validation of IMERG-GMI Version 6 Precipitation Using the GPM Validation Network. *J. Hydrometeor.*, **25 (1)**, 125–142, https://doi.org/10.1175/JHM-D-23-0134.1.

Wentz, F. J., and D. Draper, 2016: On-Orbit Absolute Calibration of the Global Precipitation Measurement Microwave Imager. *J. Atmos. Oceanic Technol.*, **33**, 1393–1412, https://doi.org/10.1175/JTECH-D-15-0212.1.

Wild, M., and Coauthors, 2015: The Energy Balance over Land and Oceans: An Assessment based on Direct Observations and CMIP5 Climate Models. *Climate Dyn.*, **44 (11-12)**, 3393–3429, https://doi.org/10.1007/s00382-014-2430-z, https://doi.org/10.1007/s00382-014-2430-z.

Wolff, D. B., and B. L. Fisher, 2009: Assessing the Relative Performance of Microwave-Based Satellite Rain-Rate Retrievals Using TRMM Ground Validation Data. *J. Appl. Meteor. Climatol.*, **48 (6)**, 1069–1099, https://doi.org/10.1175/2008JAMC2127.1.

Woods, D., P.-E. Kirstetter, H. Vergara, J. A. Duarte, and J. Basara, 2023a: Hydrologic Evaluation of the Global Precipitation Measurement Mission over the US: Error Budget Analysis. *Journal of Hydrology*, **626**, 130 212, https://doi.org/10.1016/j.jhydrol.2023.130212.

Woods, D., P.-E. Kirstetter, H. Vergara, J. A. Duarte, and J. Basara, 2023b: Hydrologic Evaluation of the Global Precipitation Measurement Mission over the US: Flood Peak Discharge and Duration. *Journal of Hydrology*, **617**, 129 124, https://doi.org/10.1016/j.jhydrol.2023.129124.

Woods, D., P.-E. Kirstetter, H. Vergara, J. A. Duarte, and J. Basara, 2024: Hydrologic Evaluation of the Global Precipitation Measurement Mission over the US: Effect of Spatial and Temporal Scales. *Journal of Hydrology*, **635**, 131 134, https://doi.org/10.1016/j.jhydrol.2024.131134.

Wu, Q., and Y. Wang, 2019: Comparison of Oceanic Multisatellite Precipitation Data from Tropical Rainfall Measurement Mission and Global Precipitation Measurement Mission Datasets with Rain Gauge Data from Ocean Buoys. *J. Atmos. Oceanic Technol.*, **36 (5)**, 903–920, https://doi.org/10.1175/JTECH-D-18-0152.1.

1097 Xie, P., R. Joyce, S. Wu, S.-H. Yoo, Y. Yarosh, F. Sun, and R. Lin, 2017: Reprocessed, Bias-
1098 Corrected CMORPH Global High-Resolution Precipitation Estimates from 1998. *J. Hydrome-*
1099 *teor.*, **18 (6)**, 1617–1641, https://doi.org/10.1175/JHM-D-16-0168.1.